Doctoral Dissertation
博士論文

Search For the Vacuum Polarization using a high-field laser and an XFEL
(高強度レーザーとＸ線自由電子レーザーを用いた真空偏極の探索)

A Dissertation Submitted for the Degree of Doctor of Philosophy
December 2020

令和２年１２月博士 (理学) 申請

Department of Physics, Graduate School of Science,
The University of Tokyo
東京大学理学系研究科物理学専攻

Yudai Seino
清野　結大

Abstract

This thesis reports a vacuum polarization search with a new experimental scheme. X-ray diffraction caused by polarized vacuum under a high laser field (vacuum diffraction, VD) is searched. In the VD experiment, the high-intensity laser pulse and the x-ray pulse are collided to diffract the x-ray. This new scheme overcomes the problem of small signal statistics in previous vacuum polarization searches. However, this scheme has not been performed since it is difficult to collide both pulses due to their small sizes (~ 1 μm) and their short pulse durations (~ 100 fs). I developed the spatially and temporally precise alignment technique to collide both pulses. In addition, I derived the theoretical formula of the signal distribution of the VD.

A first experimental search for VD was performed at the beamline 3 of SACLA, an X-ray Free Electron Laser (XFEL) facility at Hyogo, Japan. It is expected that a vacuum is polarized by the focused 0.6-TW laser field and an XFEL beam is diffracted. A precise control system of a laser phase using an adaptive optics is constructed to focus the laser pulse. A novel x-ray optics is also developed to suppress backgrounds from the XFEL beam. Both pulses are collided in head-on collision geometry using the developed alignment techniques, and diffracted x rays are searched. No significant signal is observed, and the upper limit of VD is obtained with 90% C.L. The limit is obtained as the ratio of the number of the observed x rays, $n_{\mathrm{xray,sum}} = (1.02 \pm 1.07) \times 10^4$ photons, to the number of the expected x rays in quantum electrodinamics, $n_{\mathrm{QED,sum}} = (3.9^{+6.1}_{-2.5}) \times 10^{-14}$ photons, as follows:

$$\frac{n_{\mathrm{xrays,sum}}}{n_{\mathrm{QED,sum}}} < 2.3 \times 10^{18} \quad (90\%\ \mathrm{C.L.}). \tag{1}$$

This is the first limit on vacuum polarization by the VD experiment and is also the first experimental restriction on VD. The developed experimental scheme and the techniques pave the way for observation of vacuum polarization in a future experiment.

Contents

List of Figures

List of Tables

Chapter 1

Introduction

1.1 Vacuum polarization

1.1.1 Vacuum polarization and motivation for search

The discovery of the Higgs boson in 2012 shows that the vacuum is filled with quantum fields [1, 2]. This means that a vacuum is not an empty space and hides various properties. This discovery opens a new era that exploring properties of a vacuum.

Vacuum polarization (VP) is one of the most interesting vacuum properties in the quantum electrodynamics (QED), which has not been observed yet. VP is a basic radiative correction that modifies the propagation of photons in the vacuum through a virtual pair of an electron and a positron [3]. The Feynman diagram of VP is shown in Fig. 1.1. Due to the effect of VP, photons are able to interact with each other, though a photon does not have an electric charge. A photon-photon interaction causes various physical phenomena [4]. The representative phenomenon is a photon-photon scattering, that is a scattering process of two photons (Fig. 1.2 (a)). A polarization flip and diffraction of a propagating photon in a vacuum are also caused by a photon-photon interaction (Fig. 1.2 (b)).

Since VP is a fundamental process in QED, the confirmation of it is important. However, it has not been observed yet in a vacuum. Many experiments have been performed using a laser or a magnet [5–9] to observe VP via the phenomena caused by VP. However, anyone has not observed because of its small probability of the interaction.

The phenomena caused by VP also provide a probe for a new physics. As a new particle beyond the standard model, some particles are predicted, for example, Axion, axion-like particles and millicharged particles [10–12]. The phenomena caused by VP are easily affected by these particles since these particles have an effective coupling to two photons. Therefore, we can search for these particles with the search of the phenomena caused by VP.

The observation of VP is also the verification of physics under a strong electromagnetic field. Behaviors of photons and electrons under a strong electromagnetic

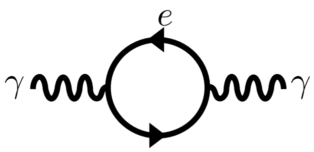

Figure 1.1: Vacuum polarization loop in QED. Wavy lines and a circle represent photons and virtual electron-positron, respectively.

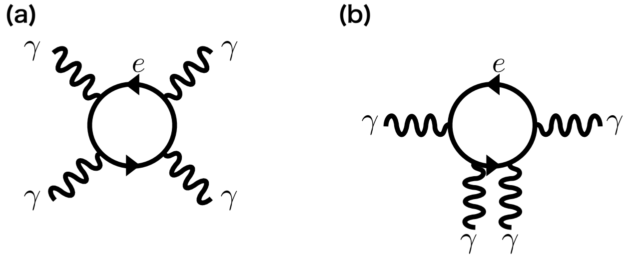

Figure 1.2: Processes of photon-photon interaction at the lowest-order QED in a vacuum. (a) Photon-photon scattering. Two photons are collided and scattered. (b) Vacuum diffraction and vacuum birefringence. A photon interacts with two photons in an electromagnetic fields.

field have not been studied, and various phenomena are predicted, for example, Shwinger effect that electrons are created by a strong electromagnetic field [13], and Unruh effect that accelerated charged particles will feel a thermal bath [14]. Strength of the interaction of a photon and an electron under a strong electromagnetic field is important to estimate these phenomena and can be measured by observing VP. Therefore, the observation of VP is the first step of the verification of these predicted phenomena.

1.1.2 Properties

The properties of VP is mathematically expressed as the Euler-Heisenberg effective lagrangian [15]. It is an effective lagrangian for the non-linear dynamics of an electromagnetic field in the QED vacuum. The lagrangian is written in Eq. (1.1) with assumptions that photon energies are well below the electron mass m_e and electromagnetic field strengths are much smaller than the QED critical values (electric field $E \ll 1.3 \times 10^{18}$ Vm^{-1}, magnetic field $B \ll 4.4 \times 10^{9}$ T),

$$\mathcal{L} = \frac{1}{2\mu_0}\left(\frac{E^2}{c^2} - B^2\right) + \frac{A_e}{\mu_0}\left[\left(\frac{E^2}{c^2} - B^2\right)^2 + 7\left(\frac{\boldsymbol{E}}{c} \cdot \boldsymbol{B}\right)^2\right], \tag{1.1}$$

where

$$A_e = \frac{2\alpha^2\hbar^3}{45\mu_0 m_e^4 c^5} = 1.32 \times 10^{-24}\ [\mathrm{T}^2] \tag{1.2}$$

with the magnetic permeability of vacuum μ_0, the speed of light in vacuum c, reduced Planck constant $\hbar$ and fine structural constant α. The second term represents the effect of VP and causes photon-photon interactions.

A change of a refractive index of a vacuum caused by VP under an electromagnetic field is written as [16]

$$n = 1 + A_e \left\{ 7 \left[(\hat{\boldsymbol{e}}_e \cdot \boldsymbol{B}) + \left(\hat{\boldsymbol{e}}_b \cdot \frac{\boldsymbol{E}}{c} \right) \right]^2 + 4 \left[(\hat{\boldsymbol{e}}_b \cdot \boldsymbol{B}) - \left(\hat{\boldsymbol{e}}_e \cdot \frac{\boldsymbol{E}}{c} \right) \right]^2 \right\}, \tag{1.3}$$

where $\hat{\boldsymbol{e}}_e$ and $\hat{\boldsymbol{e}}_b$ are unit vectors of electro and magnetic field of a propagating photon, respectively.

Due to the property of VP, three phenomena are caused (Fig. 1.2). The first is photon-photon scattering which is an elastic scattering of two photons [17]. The second is vacuum birefringence which is a phenomenon that a refractive index of a vacuum has birefringence under an electromagnetic field. The third is vacuum diffraction (VD) which is a diffraction of a photon propagating in a vacuum. Under a local electromagnetic field, the vacuum has the gradient of the refractive index, and photons propagating in that local electromagnetic field are diffracted. We can search for VP by observing these phenomena.

1.2 Previous searches for vacuum polarization

Many experimental groups have searched for VP by measuring the phenomena caused by VP,, as shown in this section. However, mainly due to an insufficient statistic of signals, anyone has not observed yet.

1.2.1 Photon-photon scattering experiment

Signature of photon-photon scattering

When the photon energy in the center of mass system, ω_{cms}, is less than the energy of an electron mass, the differential cross-section of the scattering of two photons with the same linear polarization is given by [18, 19],

$$\left(\frac{\mathrm{d}\sigma_{\gamma\gamma\to\gamma\gamma}}{\mathrm{d}\Omega} \right)_{\mathrm{QED}} = \frac{\alpha^2 r_e^2}{(180\pi)^2} \left(\frac{\omega_{\mathrm{cms}}}{m_e c^2} \right)^6 \times (260 \cos^4 \theta_{\mathrm{scat}} + 328 \cos^2 \theta_{\mathrm{scat}} + 580), \tag{1.4}$$

$$\sigma_{\mathrm{QED}} = 3.5 \times 10^{-70} (\omega_{\mathrm{cms}}\ [\mathrm{eV}])^6 \quad [\mathrm{m}^2], \tag{1.5}$$

where $r_e = e^2/4\pi\epsilon_0 m_e c^2$ is the classical electron radius, and θ_{scat} is the scattering angle in the center of mass system. The cross-section is proportional to the sixth power of ω_{cms}.

Experiments and problems

Two lasers are collided in photon-photon scattering experiments. A signal is a scattered photon, and two patterns of an experimental scheme are taken to obtain signal statistic. One scheme is the use of a laser whose pulse has many photons [5, 20, 21]. A high-field optical laser is used. Another is the use of high energy photons, which has a large cross-section [6,22]. An x-ray free electron laser (XFEL) which is a strong intensity x-ray laser is used. In both scheme experiments, lasers are focused to enhance signals. For example, the size of the focused optical lasers is 4 μm, and that of the XFEL beams is 2×200 μm in the latest experiments [6,21], respectively. Experimental parameters of these latest experiments are summarized in Tab. 1.1.

However, signal statistics obtained by these experiments are not enough though the pulse energy of both latest experiments (100 mJ and 1 μJ for [21] and [6], respectively) is a very strong class as the laser with each wavelength. Expected signals are very small and are about $\sim 10^{-19}$ photons during data acquisition. The number of background (BG) photons was expected to be $\mathcal{O}(1-10)$ photons. The observation of the photon-photon scattering using existing devices is statistically difficult.

Table 1.1: The summary of the latest photon-photon experiments. σ_{limit} is the obtained limit of the cross-section of photon-photon scattering.

Experiment	D. Bernard, et. al. [21]	T. Yamaji, et. al. [6]
Device	100 mJ optical laser	1 μJ XFEL
ω_{cms}	0.4 eV	6.5 keV
$\sigma_{\text{limit}}/\sigma_{\text{QED}}$	8×10^{17}	7×10^{19}
Expected signals	7×10^{-18} photons/100 seconds	3×10^{-19} photons/34 hour
Detector	Spectrometer	Germanium detector
Problems	· Insufficient statistic of signals · BG photons from residual gas (66 photons/100 seconds)	· Insufficient statistic of signals · BG photons of environmental radiation (0.4 photons/34 hour)

1.2.2 Vacuum birefringence experiment

Signature of vacuum birefringence

Vacuum birefringence has been searched for by pumping the vacuum with magnets. Under a magnetic field $\boldsymbol{B}$, the horizontal and the vertical refractive indices of the vacuum and their difference are described as [16]

$$n_{\parallel} = 1 + 7A_e B^2 \qquad \text{for } \hat{\boldsymbol{e}}_e \parallel \boldsymbol{B} \tag{1.6}$$

$$n_{\perp} = 1 + 4A_e B^2 \qquad \text{for } \hat{\boldsymbol{e}}_e \perp \boldsymbol{B} \tag{1.7}$$

$$\Delta n = n_{\parallel} - n_{\perp} = 3A_e B^2 \fallingdotseq 4 \times 10^{-24} B^2 \quad [\mathrm{T}^2] \tag{1.8}$$

where $\hat{\boldsymbol{e}}_e$ is the polarization vector of a propagating photon in the magnetic field. Since the refractive index depends on the direction of the magnetic field, the vacuum has birefringence.

Experiments and Problems

Some groups have searched for vacuum birefringence [9, 23, 24] (Tab. 1.2). In these experiments, a linearly polarized optical laser probes the vacuum which has birefringence due to a magnetic field of a magnet. Signals are laser lights whose polarization are changed, and the amount of the signals is proportional to B^2L, where L is a length of the magnetic field. A high-finesse optical cavity, whose mirror reflects a laser light about 10^6 times, is used to enhance a slit signal in a single path.

It seems to be difficult to improve their sensitivity by the cavity. A fake signal is generated every time when the laser light is reflected on the cavity mirror and limits the current sensitivity. They have studied the origins of the fake signal, and the strong candidate is birefringence of a mirror coating [7] or vibrations of the mirror smaller than 1 pm [8]. Because these origins are unavoidable for the mirror, the reduction of the fake signal seems to be difficult.

The improvement of the sensitivity by increasing the magnetic field is also difficult because they already use world-class strong magnets (about 10 T). Another way to increase the signals without the cavity is required, and the VD experiment is considered. Table. 1.3 shows experimental sensitivities of previous experiment against VP. The signals expected by QED, which is proportional to the square of the fine structure constant α^2, is normalized to 1, and a sensitivity to the signals are shown with 90% C.L.

Table 1.2: The summary of vacuum birefringence experiments. A_{limit} is an obtained 1σ limit of A_e.

Experiment	PVLAS [7,23]	BMV [8,24]	OVAL [9]
Magnet type	permanent	pulsed	pulsed
Magnetic field	2.5 T	6.5 T	9.0 T
Field length	1.6 m	0.1 m	0.2 m
$A_{\mathrm{limit}}/A_{\mathrm{e}}$	1×10^1	4×10^3	4×10^5
Problems	· Birefringence of cavity mirror coating	· Vibration of cavity mirrors	· Not identified

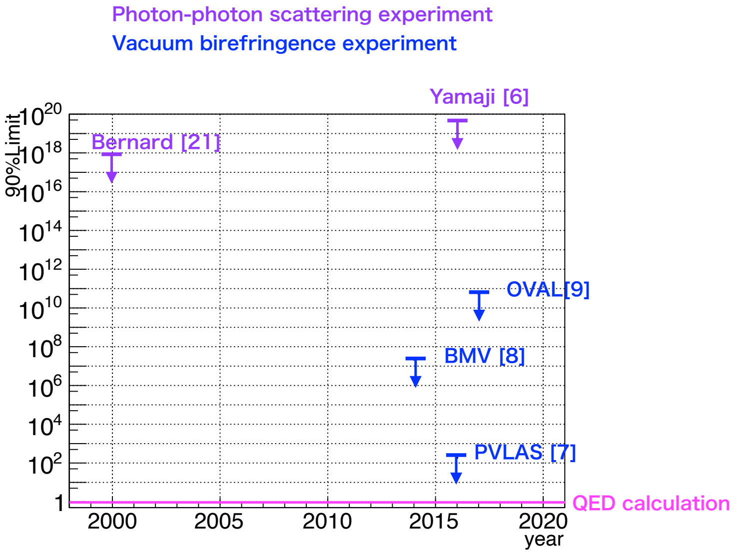

Figure 1.3: Comparison of experimental sensitivities previous experiments against VP.

1.3 Vacuum diffraction experiment using high-field laser and XFEL

Vacuum diffraction (VD) and search method

Another method to observe VP has been considered, and the search for VD was proposed in 2006 [25]. Probe photons are diffracted under a local electromagnetic field, and then diffracted probe photons are searched.

A high-field femtosecond (fs) optical laser is used to locally pump the vacuum. A focused fs laser pulse generates a locally and instantaneously strong field. As a probe light, the x-ray pulse of XFELs is used. Because the XFEL pulse is also fs laser pulse, the XFEL pulse can probe the instantaneously pumped vacuum.

Benefits of vacuum diffraction experiment

Traditionally, VP has been searched for by the photon-photon scattering experiment or the vacuum birefringence experiment. In 2009, the first XFEL was constructed, and it enabled us to perform the VD experiment.

There are benefits in the VD experiment. The VD experiment can obtain large signal statistics, which were small in previous VP experiments. An electromagnetic field of a focused laser (for example, $\mathcal{O}(10^6)$T with a peta-watt (PW) class laser) is significantly stronger than that of the magnets ($\mathcal{O}(1\text{–}10)$T). Since the signal statistics are proportional to the fourth power of the electromagnetic field, large signal statistics are generated. Furthermore, even larger signal statistics are generated by using x-ray as the probe light instead of an optical laser. The signal statistics in VD and vacuum birefringence experiments are proportional to the square of the wavenumber of probe photons. Since the wavenumber of the x-ray is four digits larger than the visible light, the signal statistics increase about 10^8 times. Observable signals are given without an optical cavity, and $\mathcal{O}(1)$ photons of VD signals are expected by one collision of the PW laser pulse and the XFEL pulse.

Another benefit is the applicability of the experimental method of the VD experiment. Since the strong pumping field of the laser can excite other quantum fields which are hidden in the vacuum, the pump-probe method can be applied to experiments to search for the unknown fields, for example, axion and millicharged particle [10–12].

We have performed the first VD experiment in the world. First VD experiment in the world is challenging and important because it creates a new way for VP search.

1.4 Outline of this thesis

In this thesis, I report the first experimental search for VD. The XFEL of SPring-8 angstrom compact free electron laser (SACLA) [26] was used as the probe laser, and a 0.6-TW laser was used as the pump laser. Both fs pulses were collided in the head-on geometry, and the first experimental limit on the VD probability was obtained.

In Chapter 2, a formula of VD signal is calculated. The detail experimental setup is explained in Chapter 3. Developed alignment methods of the XFEL pulse and the laser pulse are shown in Chapter 4, and the experimental result is shown in Chapter 5. The discussion about the result and a future experiment is shown in Chapter 6, and then I conclude the thesis in Chapter 7.

Chapter 2

Formula of Vacuum Diffraction signal

Formulae of VD signal have been calculated under various situations [27–33]. In this chapter, I derive the formulae of the signal for my experiment, which is a head-on geometry illustrated in Fig. 2.1. Details of the calculation in this chapter were published [34].

2.1 Vacuum diffraction formula

2.1.1 Assumed setup

A so-called "pump-probe" setup illustrated in Fig. 2.1 is considered. The electrical field amplitude of the XFEL pulse is

$$\begin{aligned}\mathcal{J}(\boldsymbol{x}) =& \mathcal{J}_0 \cos(k(\mathcal{Z} - ct) + \psi_0) \exp\left[-\frac{(\mathcal{Z}/c - t)^2}{(\tau_\mathrm{X}/2)^2}\right] \\ & \times \exp\left[-\frac{\mathcal{X}^2}{w_\mathrm{Xh}^2}\right] \exp\left[-\frac{\mathcal{Y}^2}{w_\mathrm{Xv}^2}\right], \end{aligned} \tag{2.1}$$

with

$$\begin{pmatrix} \mathcal{X} \\ \mathcal{Y} \\ \mathcal{Z} \end{pmatrix} = \cos\Theta \begin{pmatrix} 1 + \frac{\tan^2\Theta_y}{\tan^2\Theta}(\frac{1}{\cos\Theta} - 1) & -\frac{\tan\Theta_x \tan\Theta_y}{\tan^2\Theta}(\frac{1}{\cos\Theta} - 1) & -\tan\Theta_x \\ -\frac{\tan\Theta_x \tan\Theta_y}{\tan^2\Theta}(\frac{1}{\cos\Theta} - 1) & 1 + \frac{\tan^2\Theta_y}{\tan^2\Theta}(\frac{1}{\cos\Theta} - 1) & -\tan\Theta_y \\ \tan\Theta_x & \tan\Theta_x & 1 \end{pmatrix} \begin{pmatrix} x \\ y \\ z \end{pmatrix}, \tag{2.2}$$

where $\mathcal{J}_0$ is the peak field strength, τ_X is the pulse duration, k is the wavenumber of the x-ray, and ψ_0 is a constant phase. The $\mathcal{X}, \mathcal{Y}$ and $\mathcal{Z}$-axes are the rotated x, y and z-axes by Θ. The XFEL pulse propagates in the $\mathcal{Z}$-direction and has an incident angle, Θ, against z-axis. Θ_x (Θ_y) denotes the incident angle between $\mathcal{Z}$-axis and the y-z (x-z) plane, and satisfies $\frac{1}{\cos^2\Theta} = 1 + \tan^2\Theta_x + \tan^2\Theta_y$. Equation (2.1)

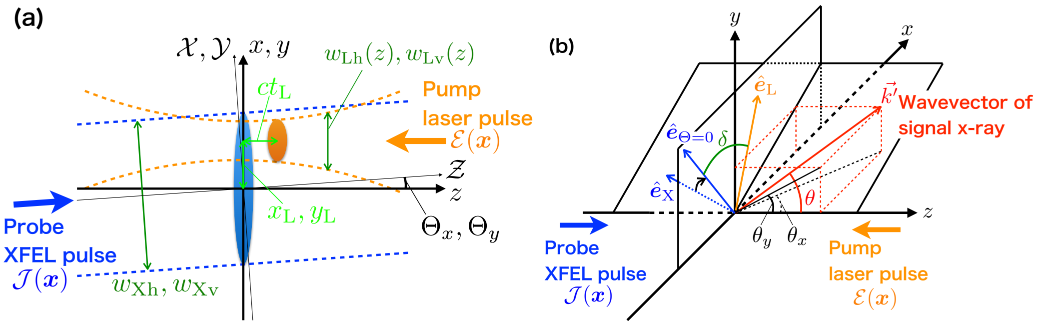

Figure 2.1: Schematic views of the experimental conditions. The XFEL pulse and the laser pulse collide in the head-on geometry. (a) Magnified view from the side around the collision point. The laser pulse propagates in the negative direction of the z-axis. The $\mathcal{Z}$-axis is the beam axis of the XFEL pulse. The XFEL pulse has incident angles, Θ_x and Θ_y, from the z-axis, and its beam size has been modelled to be constant. The laser focus has transversal displacements $(x_{\mathrm{L}}, y_{\mathrm{L}})$ from the z-axis. (b) Bird's eye view. $\hat{\boldsymbol{e}}_{\mathrm{X}}$ $(\hat{\boldsymbol{e}}_{\mathrm{L}})$ is the polarization vector of the XFEL (laser) pulse. $\hat{\boldsymbol{e}}_{\Theta=0}$, which is on the x-y plane, is the polarization vector of the XFEL pulse without the incident angle. δ is an angle between $\hat{\boldsymbol{e}}_{\mathrm{L}}$ and $\hat{\boldsymbol{e}}_{\Theta=0}$. $\vec{k'}$ is the wavevector of the signal x-ray with a diffraction angle, θ, from the z-axis. θ_x (θ_y) is an angle of θ in the x-z $(y$-$z)$ plane.

corresponds to a Gaussian beam with infinite Rayleigh length, which has constant beam sizes, w_{Xh} and w_{Xv}, in the horizontal and the vertical directions, respectively. The assumption that the beam sizes are constant is reasonable for the calculation of VD because the beam sizes are almost constant during the interaction due to the long Rayleigh length of the XFEL pulse. Typically, an XFEL beam has Rayleigh length of 0.01 m with the divergence of 100 μrad and the focal spot of 1 μm.

The laser pulse is also modelled as a pulsed beam with an electrical field amplitude,

$$\begin{aligned}\mathcal{E}(\boldsymbol{x}) =& \mathcal{E}_0 \cos(\Phi(\boldsymbol{x})) \exp\left[-\frac{(z/c + t - t_{\mathrm{L}})^2}{(\tau_{\mathrm{L}}/2)^2}\right] \\ & \times \sqrt{\frac{w_{\mathrm{L0h}}}{w_{\mathrm{Lh}}(z)}} \exp\left[-\frac{(x - x_{\mathrm{L}})^2}{w_{\mathrm{Lh}}(z)^2}\right] \times \sqrt{\frac{w_{\mathrm{L0v}}}{w_{\mathrm{Lv}}(z)}} \exp\left[-\frac{(y - y_{\mathrm{L}})^2}{w_{\mathrm{Lv}}(z)^2}\right],\end{aligned} \tag{2.3}$$

where $\mathcal{E}_0$ is the peak field strength. $\Phi(\boldsymbol{x})$ is a term which denotes a phase of the beam, and τ_{L} is the pulse duration. $w_{\mathrm{Lh}}(z)$ and $w_{\mathrm{Lv}}(z)$ are the horizontal and vertical beam sizes as a function of z, respectively, and w_{L0h} and w_{L0v} are values at the focus of the beam. The beam is focused on the x-y plane, and the focus has the horizontal and vertical displacements, x_{L} and y_{L}, from the origin. t_{L} is time of a delay of the laser pulse.

Since the photon-photon interaction due to VD is almost unaffected by the wavelength of the pump laser, the oscillating term $\cos(\Phi(\boldsymbol{x}))$ in Eq. (2.3), which depends on the wavelength of the pump laser, can be averaged over the oscillation of the laser field [28,29]. This gives $\cos^2(\Phi(\boldsymbol{x})) \to \frac{1}{2}$. I calculate the pulse energy of the laser, W, to express the peak intensities, $\mathcal{E}_0^2$ and $\mathcal{J}_0^2$, with measurable quantities as $W = \int \mathrm{d}x\mathrm{d}y\mathrm{d}z\epsilon_0\mathcal{E}^2(\boldsymbol{x}) \simeq \epsilon_0\frac{(2\pi)^{3/2}\mathcal{E}_0^2 w_{\mathrm{L0h}} w_{\mathrm{L0v}} c\tau_{\mathrm{L}}}{32}$, where ϵ_0 is the dielectric constant. From this, the peak intensities can be written as $\mathcal{E}_0^2 \simeq \frac{32W}{(2\pi)^{3/2}\epsilon_0 w_{\mathrm{L0h}} w_{\mathrm{L0v}} c\tau_{\mathrm{L}}}$ and $\mathcal{J}_0^2 \simeq \frac{32N\hbar ck}{(2\pi)^{3/2}\epsilon_0 w_{\mathrm{Xh}} w_{\mathrm{Xv}} c\tau_{\mathrm{X}}}$, where N is the number of x rays in the XFEL pulse and $\hbar ck$ is photon energy of the x-ray.

2.1.2 Signal formula

In the assumed setup, an interaction probability of VD for each x-ray, P, is written as [29],

$$\begin{aligned}\frac{\mathrm{d}^3P}{k'^2\mathrm{d}k'\mathrm{d}\phi\mathrm{d}\cos\theta} =& \frac{1}{N}\frac{2^2}{45^2\pi^3}\frac{\alpha^4\hbar^5\epsilon_0^3}{m_e^8c^9}k'(1+\cos\theta)^2(16+33\sin^2\delta)\\ &\times {\mathcal{J}_0}^2{\mathcal{E}_0}^4|\mathcal{M}|^2,\end{aligned} \tag{2.4}$$

with

$$\mathcal{M} = \int \mathrm{d}^4\mathscr{X}\,\exp\left(i\mathscr{K}'\mathscr{X}\right)\frac{\mathcal{J}(\boldsymbol{x})}{\mathcal{J}_0}\left(\frac{\mathcal{E}(\boldsymbol{x})}{\mathcal{E}_0}\right)^2, \tag{2.5}$$

where $\mathscr{X} = (ct, \boldsymbol{x}) = (ct, x, y, z)$ and $\mathscr{K}' = (k', \vec{k'})$ are four-vectors with the metric $(-1, 1, 1, 1)$, and $k' = |\vec{k'}|$. $\vec{k'} = k'(\sin\theta\cos\phi, \sin\theta\sin\phi, \cos\theta) = k'\cos\theta(\tan\theta_x, \tan\theta_y, 1)$ is the wavevector of the diffracted x-ray, which is the signal. θ is the diffraction angle of the signal x-ray from the z-axis. δ, which is illustrated in Fig. 2.1 (b), is the angle between the polarization vector of the laser pulse, $\hat{\boldsymbol{e}}_{\mathrm{L}}$, and a vector, $\hat{\boldsymbol{e}}_{\Theta=0}$, where $\hat{\boldsymbol{e}}_{\Theta=0}$ is a polarization vector of the XFEL pulse without the incident angle.

The calculation is performed with realistic approximations [34]. One of the important approximation is against the pulse durations. The pulse durations of typical fs lasers and XFELs are short and satisfy $c\tau_{\mathrm{L}} \ll z_{\mathrm{RL}}$ and $c\tau_{\mathrm{X}} \ll z_{\mathrm{RL}}$, where z_{RL} is Rayleigh length of the laser beam. For example, the pulse length of typical fs lasers satisfies $c\tau_{\mathrm{L}} < 30$ μm ($\tau_{\mathrm{L}} < 100$ fs), and $c\tau_{\mathrm{X}}$ is much shorter than that, whereas z_{RL} is $\sim 400\mu$m for 10 μm of the minimum beam size and $\lambda = 800$ nm of the wave length. In this short-pulse condition, we can approximate $w_{\mathrm{L}i}(z)$ to be constant during the interaction as $w_{\mathrm{L}i}(z) = w_{\mathrm{L}i}(ct_{\mathrm{L}}/2) \simeq w_{\mathrm{L}i}$ $(i = \mathrm{h}, \mathrm{v})$. The interaction probability, P, is approximately calculated as

$$\begin{aligned}\frac{\mathrm{d}P}{\mathrm{d}\cos\theta} =&\frac{2^6}{45^2\pi^2}\frac{\alpha^4\hbar^6}{m_e^8c^{10}}(16+33\sin^2\delta)k^2W^2\\ &\times\frac{1}{w_{\mathrm{Lh}}w_{\mathrm{Lv}}}\frac{1}{\sqrt{w_{\mathrm{Lh}}^2+2w_{\mathrm{Xh}}^2}}\frac{1}{\sqrt{w_{\mathrm{Lv}}^2+2w_{\mathrm{Xv}}^2}}\\ &\times\exp\left[-4\frac{x_{\mathrm{L}}^2}{w_{\mathrm{Lh}}^2+2w_{\mathrm{Xh}}^2}-4\frac{y_{\mathrm{L}}^2}{w_{\mathrm{Lv}}^2+2w_{\mathrm{Xv}}^2}\right]\\ &\times\frac{k}{\sqrt{2\pi}}\sqrt{\frac{w_{\mathrm{Lh}}^2w_{\mathrm{Xh}}^2}{w_{\mathrm{Lh}}^2+2w_{\mathrm{Xh}}^2}}\exp\left[-\frac{1}{2}\frac{w_{\mathrm{Lh}}^2w_{\mathrm{Xh}}^2}{w_{\mathrm{Lh}}^2+2w_{\mathrm{Xh}}^2}k^2(\theta_x-\Theta_x)^2\right]\\ &\times\frac{k}{\sqrt{2\pi}}\sqrt{\frac{w_{\mathrm{Lv}}^2w_{\mathrm{Xv}}^2}{w_{\mathrm{Lv}}^2+2w_{\mathrm{Xv}}^2}}\exp\left[-\frac{1}{2}\frac{w_{\mathrm{Lv}}^2w_{\mathrm{Xv}}^2}{w_{\mathrm{Lv}}^2+2w_{\mathrm{Xv}}^2}k^2(\theta_y-\Theta_y)^2\right].\end{aligned}\tag{2.6}$$

By assuming a symmetrical beam shape ($w_{\mathrm{Xh}}=w_{\mathrm{Xv}}=w_{\mathrm{X}}$ and $w_{\mathrm{Lh}}=w_{\mathrm{Lv}}=w_{\mathrm{L}}$), I shows the more simple formula. The formula becomes

$$\begin{aligned}\frac{\mathrm{d}P}{\mathrm{d}\cos\theta} =&\frac{2^6}{45^2\pi^2}\frac{\alpha^4\hbar^6}{m_e^8c^{10}}(16+33\sin^2\delta)k^2W^2\\ &\times\frac{1}{w_{\mathrm{L}}^2(w_{\mathrm{L}}^2+2w_{\mathrm{X}}^2)}\times\frac{2}{\pi w^2}\int I_{\mathrm{IV}}(x,y)\mathrm{d}x\mathrm{d}y\\ &\times(kw)^2\exp\left[-\frac{1}{2}(kw)^2\{(\theta_x-\Theta_x)^2+(\theta_y-\Theta_y)^2\}\right],\end{aligned}\tag{2.7}$$

with

$$w=\frac{w_{\mathrm{L}}w_{\mathrm{X}}}{\sqrt{w_{\mathrm{L}}^2+2w_{\mathrm{X}}^2}},\tag{2.8}$$

$$\begin{aligned}I_{\mathrm{IV}}(x,y)=&\exp\left[-2\frac{x^2+y^2}{w_{\mathrm{X}}^2}\right]\\ &\times\left(\exp\left[-2\frac{(x-x_{\mathrm{L}})^2+(y-y_{\mathrm{L}})^2}{w_{\mathrm{L}}^2}\right]\right)^2,\end{aligned}\tag{2.9}$$

It consists of three parts; the parameter dependency part (the first line of Eq.(2.7)), the form part of the two pulses (the second line) and the angular distribution part (the third line). It provides a valuable approximation to understand VD and to optimize experimental setups since the parameter dependence of the interaction probability is clear.

In the second line of Eq. (2.7), $I_{\mathrm{IV}}(x,y)$ is the product of intensity distributions of the two pulses, $(\mathcal{J}(\boldsymbol{x})^2)\times(\mathcal{E}(\boldsymbol{x})^2)^2$, at the collision point. The exponents of the intensities agree with the number of photons of the leading-order Feynman diagram for VD (one x-ray and two laser photons, Fig. 1.2). This overlap of the two pulses can be thought of as an effective interaction volume. The interaction

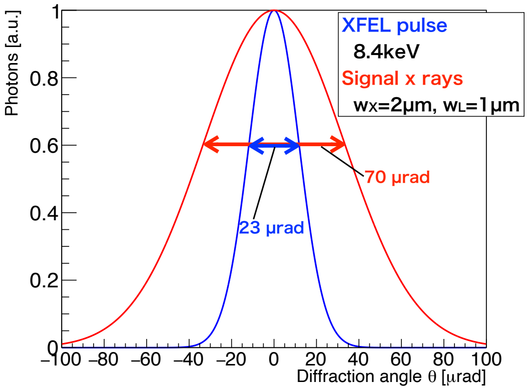

Figure 2.2: Angle distributions of the signal x rays (red line) and the probe XFEL pulse (blue line).

volume shows how good the two pulses overlap in space-time and gets decreased by large displacements, (x_L, y_L). w is the 2σ size of this interaction volume.

The third line of Eq. (2.7) shows that the angular distribution has a Gaussian profile with the signal divergence, $\frac{2}{kw}$, and the center of the distribution is the incident angle. The uncertainty principle binds a relation between the signal divergence and the size of the interaction volume in the transverse direction; $\Delta p \Delta x = \frac{1}{kw}\hbar k \times \frac{w}{2} = \frac{\hbar}{2}$. A relation between the signal divergence and the size of the interaction volume in the transverse direction is bound by the uncertainty principle as the following: $\Delta p \Delta x = \frac{1}{kw}\hbar k \times \frac{w}{2} = \frac{\hbar}{2}$.

Figure 2.2 shows angular distributions of the signal x rays (red line) and the probe XFEL pulse (blue line). For these calculations, $w_L = 1$ μm, $w_X = 2$ μm and 8.4 keV of x-ray photon energy are used. Both distributions are a Gaussian profile. Due to the effect of VD, signal divergence (70 μrad) is larger than that of the probe XFEL pulse (23 μrad).

Equation (2.7) is validated by comparing with a previous calculation [29] in [34], The ratios of the signal divergence and the interaction probability are shown in Fig. 2.3. In the calculation, perfect alignment and same pulse durations are assumed $(\Theta = 0, x_L = y_L = 0, t_L = 0,\ \tau = \tau_X = \tau_L)$. The beam sizes at the focus are assumed as 1 μm for the laser pulse and 2 μm for the XFEL pulse. For the previous calculation, a Gaussian beam and its Rayleigh length $z'_{RL} = 3.9$ μm are assumed. The calculated results show good agreement in the short pulse condition and become the same in the limit of $\tau_X, \tau_L \to 0$.

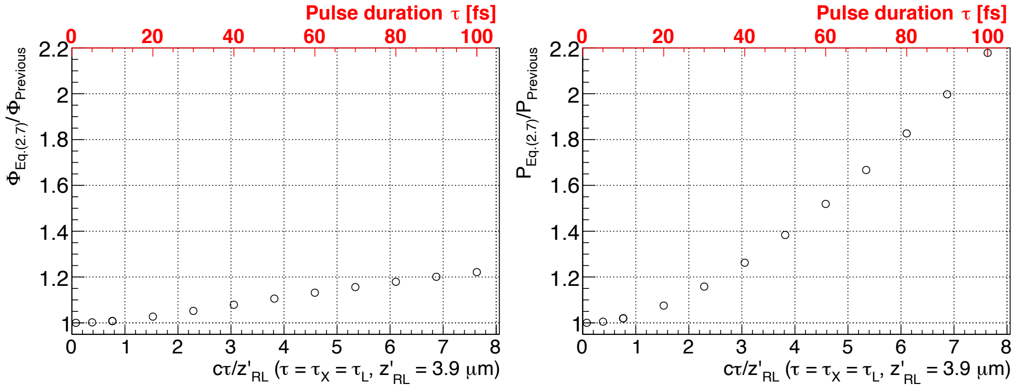

Figure 2.3: Validation of the short-pulse approximation. The signal divergence and the interaction probability calculated by Eq. (2.7), $\Phi_{\mathrm{Eq.(2.7)}}$ and $P_{\mathrm{Eq.(2.7)}}$, are compared with those calculated by the previous calculation [29], Φ_{Previous} and P_{Previous}, respectively. Left: $\Phi_{\mathrm{Eq.(2.7)}}/\Phi_{\mathrm{Previous}}$. Right: $P_{\mathrm{Eq.(2.7)}}/P_{\mathrm{Previous}}$.

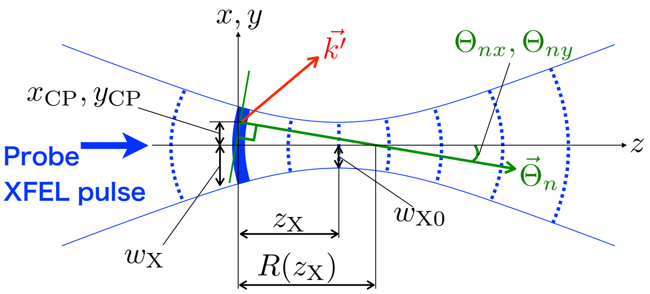

Figure 2.4: Schematic view of the focused XFEL pulse at the collision point. The XFEL pulse is away from its focus by z_{X}. The wavefront is drawn as a thick line. Θ_{nx} (Θ_{ny}) is an angle between the y-z (x-z) plane and the normal direction of the wavefront, $\vec{\Theta}_n$. These angles effectively give the incident angles to the x-ray.

2.2 Vacuum diffraction formula with XFEL curvature effect

So far, the simple formula of VD without the curvature of the XFEL pulse has been considered. However, in realistic experiments, the XFEL pulse has the curvature. The x-ray is effectively given the incident angle by the curvature. In order to estimate the effect by the curvature, the XFEL pulse as a Gaussian beam, as shown in Fig. 2.4, is considered. The beam size is given as $w_{\mathrm{X}} = w_{\mathrm{X0}}\sqrt{1 + (\frac{z_{\mathrm{X}}\varphi}{w_{\mathrm{X0}}})^2}$, where w_{X0} is a minimum beam size, z_{X} is the distance from the collision point to the focus along the z-axis, and φ is the divergence. The curvature radius of the wavefront is

$$R(z_{\mathrm{X}}) = z_{\mathrm{X}} \left(1 + \left(\frac{w_{\mathrm{X}0}}{z_{\mathrm{X}} \varphi} \right)^2 \right). \tag{2.10}$$

At a position $(x_{\mathrm{CP}}, y_{\mathrm{CP}})$ on the wavefront, which is the x-y coordinate at the collision point, the normalized normal direction, $\vec{\Theta}_n$, is given as the following:

$$\begin{aligned} \vec{\Theta}_n &= \cos\Theta_n \left(\tan\Theta_{nx}, \tan\Theta_{ny}, 1 \right) \\ &= \left(-\frac{x_{\mathrm{CP}}}{R(z_{\mathrm{X}})}, -\frac{y_{\mathrm{CP}}}{R(z_{\mathrm{X}})}, \cos\Theta_n \right) \fallingdotseq (\Theta_{nx}, \Theta_{ny}, 1), \qquad (\Theta_n \ll 1), \end{aligned} \tag{2.11}$$

where Θ_{nx} (Θ_{ny}) is an angle between the y-z (x-z) plane and the normal direction and satisfies $\frac{1}{\cos^2\Theta_n} = 1 + \tan^2\Theta_{nx} + \tan^2\Theta_{ny}$. These angles are approximately given by the x and y components of the normal direction.

Under the situation that $\Theta_n \ll 1$, the new VD formula is given by the convolution of the original angular distribution, Eq. (2.6), and the angle of the normal direction with the weight, $I_{\mathrm{IV}}(x_{\mathrm{CP}}, y_{\mathrm{CP}})$. The convolution is given by the integrations over x_{CP} and y_{CP} as

$$\frac{\mathrm{d}P_{\mathrm{curve}}}{\mathrm{d}x_{\mathrm{CP}}\mathrm{d}y_{\mathrm{CP}}\mathrm{d}\cos\theta} = \frac{I_{\mathrm{IV}}(x_{\mathrm{CP}}, y_{\mathrm{CP}})}{\int I_{\mathrm{IV}}(x_{\mathrm{CP}}, y_{\mathrm{CP}})\mathrm{d}x_{\mathrm{CP}}\mathrm{d}y_{\mathrm{CP}}} \left. \frac{\mathrm{d}P}{\mathrm{d}\cos\theta} \right|_{\Theta_x=\Theta_{nx}, \Theta_y=\Theta_{ny}}. \tag{2.12}$$

Due to the convolution, the divergence caused by the curvature at the collision point, $w/R(z_{\mathrm{X}})$, smears the original divergence, $2/kw$. The signal divergence becomes their root sum square, $\sqrt{(2/kw)^2 + (w/R(z_{\mathrm{X}}))^2}$. The center direction of the angular distribution is shifted to the normal direction at the center of the interaction volume, and the central angles become $(-2w^2 x_{\mathrm{L}}/w_{\mathrm{L}}^2 R(z_{\mathrm{X}}), -2w^2 y_{\mathrm{L}}/w_{\mathrm{L}}^2 R(z_{\mathrm{X}}))$.

Chapter 3

Setup and devices

The experiment is performed at SACLA during a beam time between 2019/06/27 10:00 and 2019/07/01 10:00 JST (96 hours). In this section, I describe the experimental setup about the probe XFEL system, the pump laser system and a signal detection system. In Tab. 3.1, main experimental parameters are summarized.

Table 3.1: The summary of main experimental parameters.

Parameters		
X-ray photon energy	$\hbar ck$	8.4 keV
XFEL beam size (Horizontal)	w_{Xh}	22.0 μm
XFEL beam size (Vertical)	w_{Xv}	14.8 μm
XFEL pulse duration	τ_{X}	17 fs
Pump laser		0.6-TW laser
Pump laser pulse energy	W	0.47 mJ
Laser beam size (Horizontal)	w_{Lh}	1.9 μm
Laser beam size (Vertical)	w_{Lv}	1.9 μm
Laser pulse duration	τ_{L}	48 fs
Signal selection angle by Slit6		38.8 μrad $< \theta_{\mathrm{y}} <$ 58.6 μrad
Collision rate		15 Hz

3.1 Probe XFEL system

3.1.1 XFEL beamline and devices

Figure 3.1 is a schematic of experimental apparatuses related to the XFEL beamline. SACLA XFEL beamline 3 (BL3) is used as the source of the probe light. The undulator of BL3, which oscillates an electron beam by a periodic magnetic field of

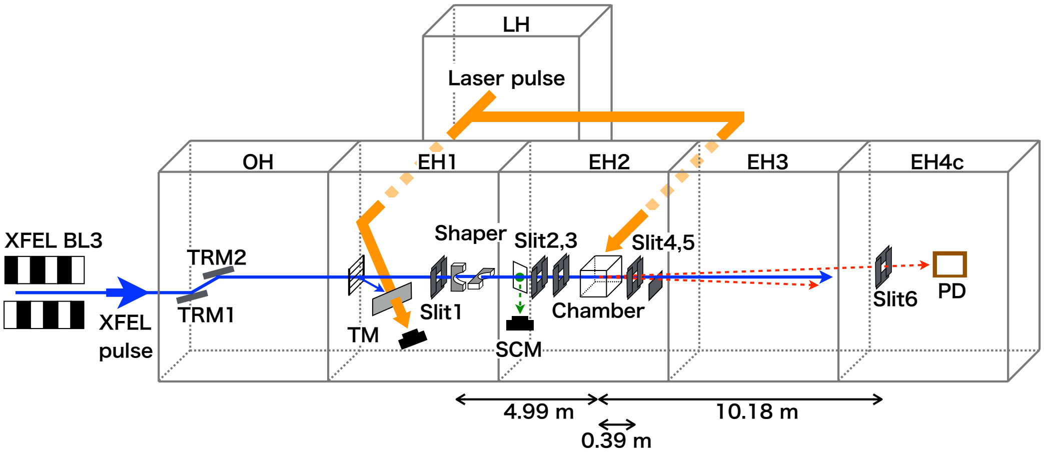

Figure 3.1: The apparatuses in SACLA BL3. All components are connected with vacuum pipes. (TRM1, TRM2: Total reflection mirrors; SCM: Beam intensity monitor; TM: Arrival timing monitor; Shaper: One-dimension x-ray lens; Chamber: Vacuum chamber in which the both beams are collided; Slit1–4,6: 4-jaw slit with tantalum blades; Slit5: Vertical slit with a tantalum blade; PD: Photodiode)

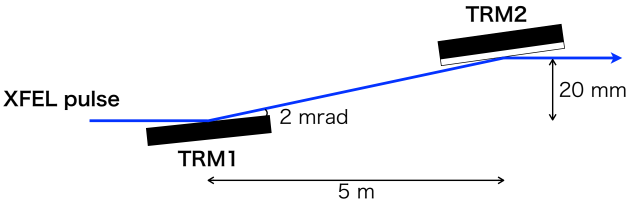

Figure 3.2: A pair of total reflection mirrors (TRM).

magnets, generates a horizontally polarized x-ray pulse with $\sim 10^{11}$ photons/pulse, and each pulse duration, τ_X, is below 17 fs [26]. The photon energy of the x-ray, $\hbar ck$, is set to 8.4 keV, and its bandwidth is 25 eV (2σ).

The XFEL pulse is collided with the laser pulse in the vacuum chamber at experimental hatch 2 (EH2). The XFEL pulse passes through the following optical devices and monitors before the collision.

Total reflection mirror (TRM)

A pair of total reflection mirrors (TRM) [35] as shown in Fig. 3.2 is used to remove the second harmonics of x rays (16.8 keV) whose contamination fraction is about $\sim 3 \times 10^{-4}$. Substrates of the TRM1 and the TRM2 are silicon (Si), and the surface of the TRM2 is coated by carbon. The incident angle of the TRM is set to 2 mrad, which corresponds to the critical angle of 15 keV x-ray. Since the critical angle is inversely proportional to x-ray photon energy, high energy photons are decreased with the reflection. The reflectivity of the two TRMs are $\sim 3 \times 10^{-2}$ for 16.8 keV

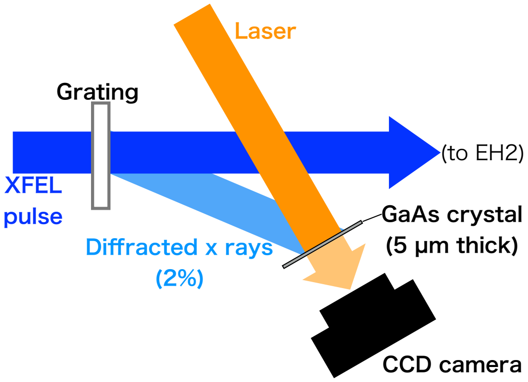

Figure 3.3: Top view of the timing monitor (TM). The relative timing of the XFEL pulse and the laser pulse is monitored by measuring the laser transmittance of the GaAs crystal.

x-ray, and the contamination is suppressed below 10^{-5} by the TRMs.

Timing monitor (TM)

A relative timing between the XFEL pulse and the pump laser pulse is measured by a timing monitor (TM) [36], as shown in Fig. 3.3. The TM consists of a transmission grating, a CCD camera and a 5-μm-thick GaAs crystal, which is glued on a 500-μm-thick sapphire substrate. 2 % of x rays in the XFEL pulse are diffracted by the grating and irradiated to the GaAs crystal. At the same time, the laser pulse is also irradiated, and a part of the laser photons are transmitted. The transmittance of the laser pulse is monitored by the CCD camera.

The relative timing of the two pulses can be measured by monitoring the laser transmittance. The GaAs crystal which absorbs x rays changes its optical transparency because x rays ionize GaAs atoms and decrease the permittivity of the GaAs crystal [36, 37]. As the result, power of the transmitted laser light changes depending on the relative timing of the XFEL pulse and the laser pulse. A resolution of the relative timing is 6 fs.

Screen monitor (SCM)

A screen monitor (SCM) is inserted on the XFEL beam axis to measure an intensity of the XFEL pulse, as shown in Fig. 3.4. The SCM consists of a CCD camera and a 30-μm-thick boron-doped diamond film. The diamond film, which is tilted at 45 degrees against the XFEL beam axis, is a fluorescence screen. The intensity of its fluorescence light, which corresponds to the intensity of the XFEL pulse, is measured by the CCD camera. The transmittance of an 8.4 keV x-ray is 95 %, and a resolution of the intensity is 3 %.

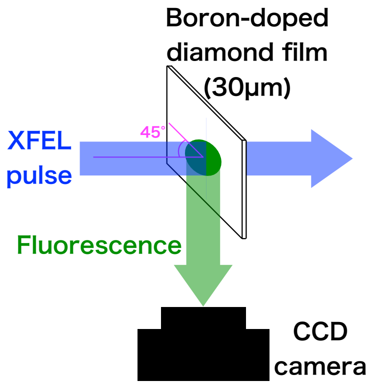

Figure 3.4: Screen monitor (SCM). The intensity of the XFEL pulse is monitored by measuring the intensity of the fluorescence of the boron-doped diamond film.

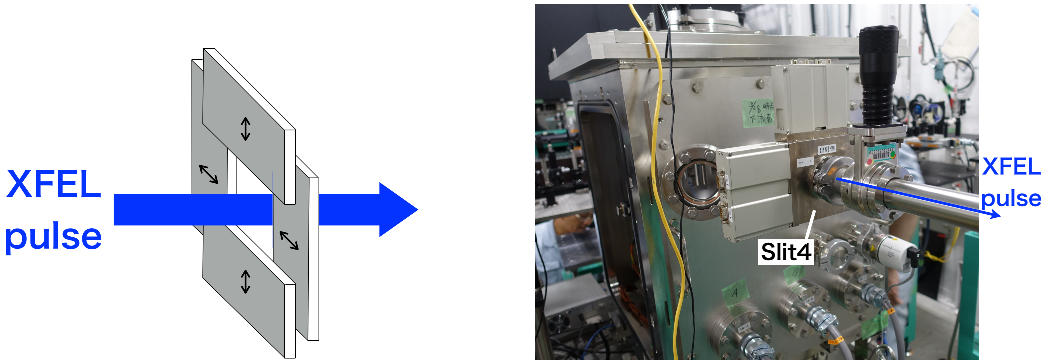

Figure 3.5: The 4-jaw slit. Left: Schematic of a 4-jaw slit. Each blade can be moved against the XFEL beam axis. Right: A side view of the Slit4. Four blades are in the container of the slit, which can be evacuated.

Slit

Slits are used for three purposes. The first purpose is to make the size of the XFEL pulse small. The second is to measure the size of the XFEL pulse. The third is to separate the diffracted x rays from the XFEL pulse. Blades of the slits are made of tantalum. Each slit is composed of four blades as shown in Fig. 3.5 Left. The fifth slit (Slit5) from the upstream position of the XFEL beamline is composed of only a lower blade. Each blade can be moved with about 1 μm step by a motorized position stage.

3.1.2 Chamber

Figure 3.6 shows the top view of the vacuum chamber. The XFEL pulse and the laser pulse are collided in the chamber. A sample stage, which is a motorized position stage, is set to study the XFEL pulse and the laser pulse properties at the

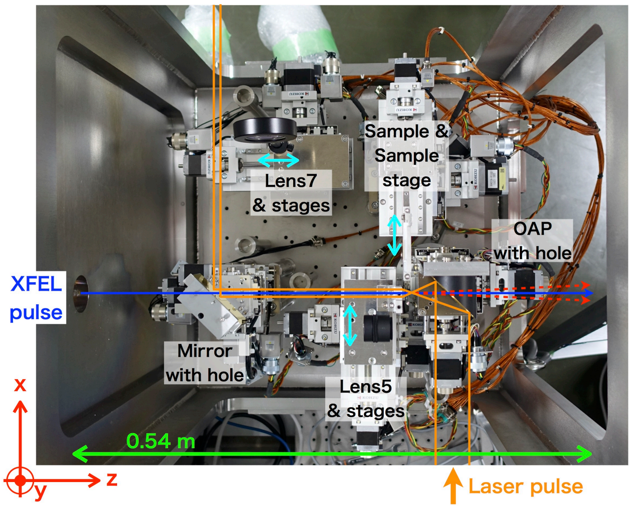

Figure 3.6: Top view of the vacuum chamber. (OAP: 90-degree off-axis parabolic mirror with a 3-mm diameter hole; Mirror: Plane mirror with a 2-mm diameter hole; Sample; A sample placed at the collision point; Lens5: Achromatic doublet lens with 10-mm focal length and 8-mm diameter; Lens7: Achromatic doublet lens with 400-mm focal length and 50.8-mm diameter) The samples, the Lens5 and the Lens7 are mounted on the motorized position stage, and these can be inserted on the laser beam axis. In the figure, the Lens5 is inserted.

collision point. A sample on a sample folder can be mounted on the sample stage and be moved in x, y and z-directions around the collision point. Figure 3.7 shows a test film and a wire on the sample folder. The chamber and the XFEL beamline were evacuated below 4×10^{-3} Pa.

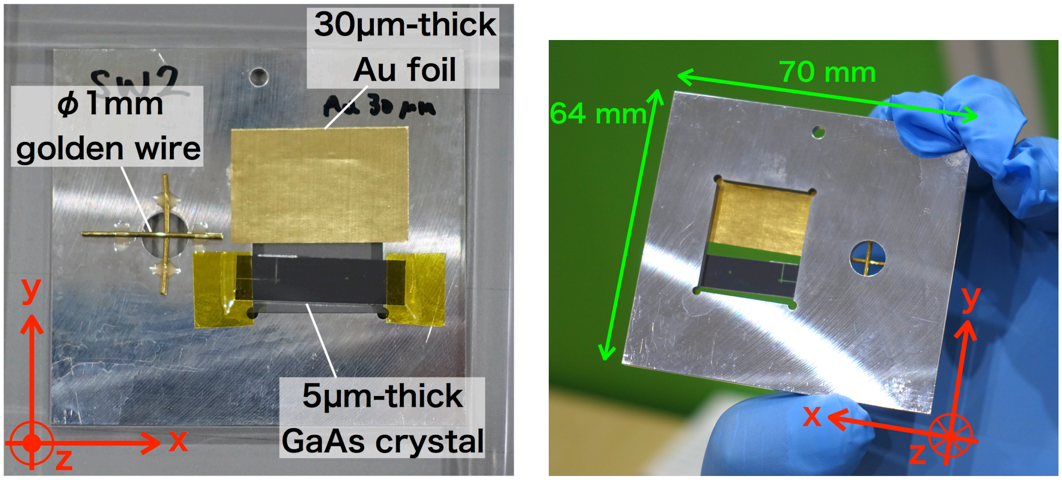

Figure 3.7: The sample folder. The 30-μm-thick Au foil, the 5-μm-thick GaAs crystal glued on a 500-μm-thick sapphire substrate and the 1 mm diameter golden wire are set on the folder. Left: Front side view of the folder. Right: Back side view of the folder.

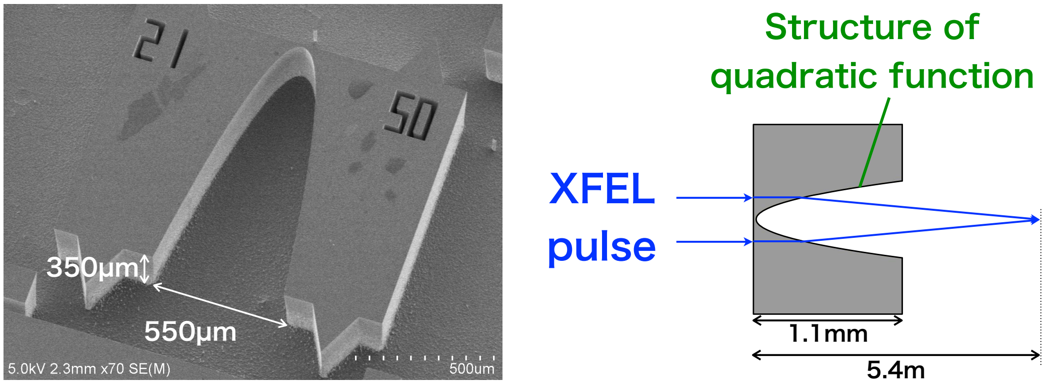

Figure 3.8: The shaper. Left: SEM image of the shaper. Right: Schematic of the shaper.

3.1.3 Shaper

The shaper is developed to suppress the BGs in the VD experiment. The shaper is a one-dimensional optical device for x rays made of a Si crystal. The shaper has been developed with Yamamura laboratory, department of precision science and technology, graduate school of engineering, Osaka University. I devised and designed the shaper. The shaper was manufactured by Yamamura laboratory and studied its performance by me. Figure 3.8 (Left) shows a scanning electron microscope(SEM) image of a shaper. A structure of quadratic function is made by a reactive ion etching method. Reactive ion etching is a kind of a dry etching, and we can make an arbitrary structure with a few hundred μm of depth. When an uniform x-ray pulse passes the shaper, its profile becomes gaussian distribution due to the attenuation by the shaper with the quadratic function structure.

There are two roles of the shaper. One role is a lens for the XFEL pulse. Since the refractive index of silicon for x rays is smaller than 1, an XFEL pulse passing through the shaper is focused as shown in Fig. 3.8 (Right). The shapers are designed with 5.4 m of a focal length (f) and 350 μm of an aperture which corresponds to the depth of the etching. Two shapers are used to focus the XFEL pulse in the horizontal and the vertical directions, respectively.

Another role is to reduce BGs. There are two main BGs. First is diffused x rays by a lens. Second is a part of probe x rays which have large divergence due to the focusing. By using a shaper, these BG x rays are suppressed or absorbed by a shaper. These effect is detailed in App. A.

Figure 3.9 shows the setup of the shapers. From the upstream side, the Slit1, the vertical focusing shaper, and the horizontal focusing shaper are placed. The shapers are mounted on the motorized position stages and inserted on the XFEL beam axis. The vacuum pipe containing the shaper is also mounted on the other motorized position stages which move in transverse directions against the beam axis, and the position of the shaper can be adjusted by the stages.

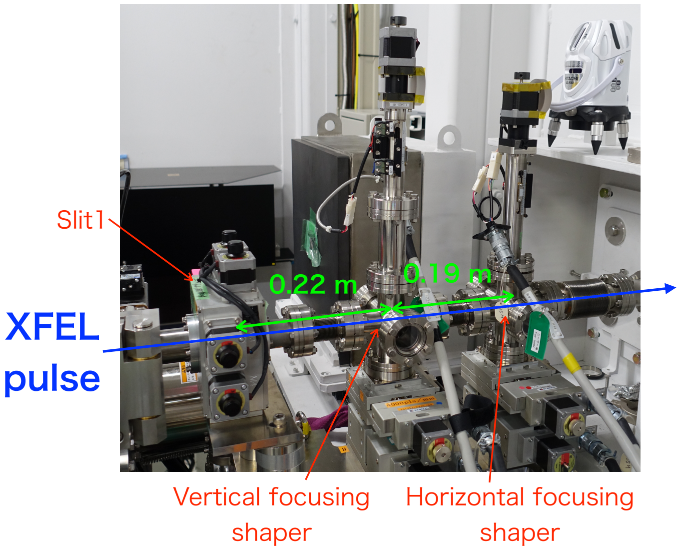

Figure 3.9: Setup of the Slit1 and the shapers at EH1. The shapers are in the vacuum pipe and mounted on the motorized position stages to be inserted on the XFEL beam axis. The distance between the Slit1 and the shaper for the vertical focusing is 0.22 m, and the distance between the two shapers is 0.19 m.

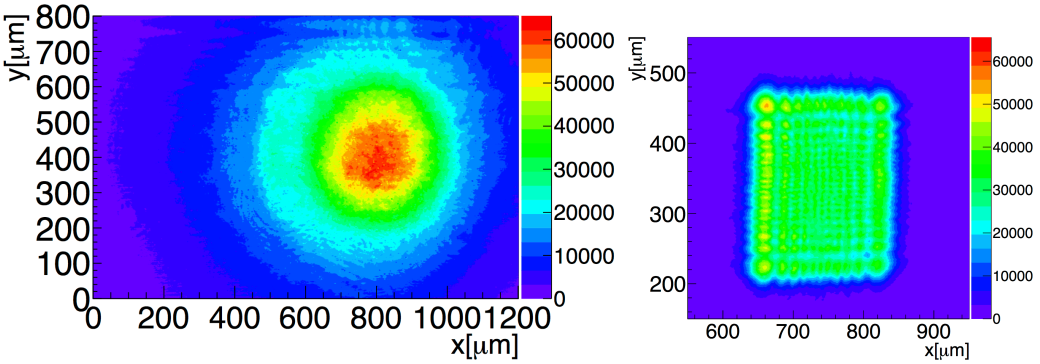

Figure 3.10: Images of the XFEL pulse with the x-ray camera. Left: Raw beam image of the XFEL pulse. Right: Image of the XFEL pulse with a collimation by Slit1.

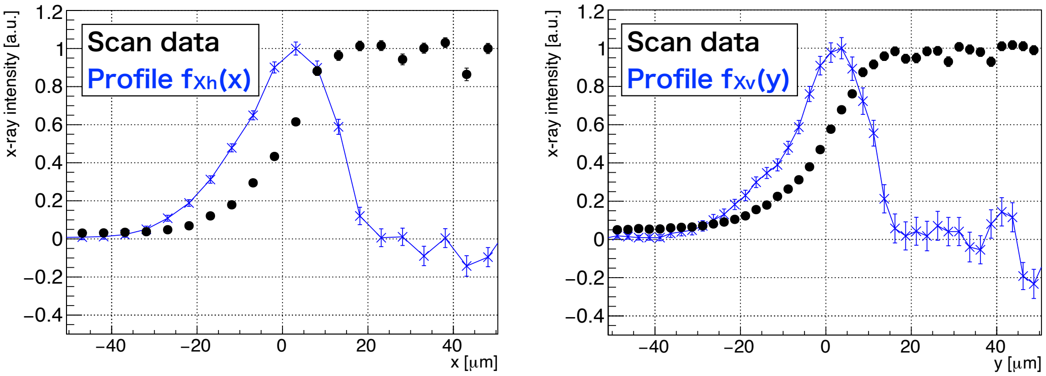

Figure 3.11: XFEL profiles at the collision point. Black markers show the intensity of the transmitted x rays during the knife-edge scan, and blue markers show the XFEL profile at the collision point. Left: In horizontal direction; Right: In vertical direction.

3.1.4 XFEL beam

Figures 3.10 shows a x-ray camera images of the original XFEL pulse without the shapers. The x-ray camera is composed of a screen of a scintillator and a CCD camera and is placed 7.5-m downstream from the shaper for a vertical focusing. The beam sizes of the original XFEL pulse (Fig. 3.10 Left) are 524 μm and 588 μm (FWHM) in the vertical and the horizontal directions, respectively. Since the original XFEL pulse is larger than the aperture of the shaper (350 μm), the XFEL pulse is cut by the Slit1 and made rectangular (Fig. 3.10 Right). The FWHM sizes of the rectangular XFEL pulse are (262 ± 3) μm and (195 ± 3) μm in the vertical and the horizontal directions, respectively, where errors show fluctuations of the sizes. This rectangular XFEL pulse is focused with the two shapers.

At the collision point, the beam sizes of the focused XFEL pulse were measured using crossed 1-mm diameter golden wires mounted on the sample stage (Fig. 3.7). The beam size was measured with the knife-edge scan method. The position of the wire was scanned, and the intensity of the transmitted x rays was measured with a PIN photodiode (PD, HAMAMATSU, S3590-09), which has 3% of an energy resolution. The wire position was scanned from four directions (from upper, lower, right, left). At each wire position, about one hundred pulses of the x-ray intensity were measured and averaged.

The distributions of the x-ray intensity in the horizontal and the vertical directions are shown in Fig. 3.11 with black points. The profile of the XFEL pulse is calculated using a slope of the intensity distribution. The profiles in the horizontal and the vertical directions are shown with blue points and defined as $f_{\mathrm{Xh}}(x)$ and $f_{\mathrm{Xv}}(y)$, respectively. The slope is evaluated with three to seven points, and blue points show the case evaluated with five points. The beam sizes in the horizontal and the vertical directions were $w_{\mathrm{Xh}} = (22.0 \pm 3.5)$ μm and $w_{\mathrm{Xv}} = (14.8 \pm 4.3)$ μm, respectively, which are 2σ beam sizes calculated from the FWHM of the profile. Dominant uncertainties of the beam size are due to the direction of the knife-edge scan and the number of points to calculate the slope. The position of the beam axis $(x = 0, y = 0)$ is defined as the position where the transmitted x rays is 50% and measured with accuracies of 3.1 μm and 1.7 μm horizontally and vertically, respectively.

The divergence of the XFEL pulse in the vertical direction was estimated by fitting the beam sizes along the beam axis. The beam sizes were measured by knife-edge scan method using the Slit2—6. The x-ray camera was also used. Positions of these devices are summarized in Tab. 3.2. Light blue points in Fig. 3.12 show the measured beam sizes. A blue line shows the fitting result of the beam sizes by the following function of a gaussian beam

$$w_{\mathrm{X}}(z) = w_{\mathrm{X0v}} \sqrt{1 + \left(\frac{(z - z_{\mathrm{X}})\varphi}{w_{\mathrm{X0v}}} \right)^2} \tag{3.1}$$

where z is a distance from collision point, z_{X} is a focal position of the XFEL pulse, w_{X0v} is a minimum beam size and φ is a divergence. Fitting results of these parameters are $z_{\mathrm{X}} = (1.76 \pm 0.08)$ m, $w_{\mathrm{X0v}} = (3.1 \pm 1.8)$ μm and $\varphi = (10.6 \pm 1.1)$ μrad.

Table 3.2: Positions of shapers, slits and the x-ray camera from the collision point.

Devices	z [m]
Slit1	-5.22
Shaper for vertical focusing	-4.99
Shaper for horizontal focusing	-4.81
Slit2	-2.11
Slit3	-0.99
Collision point	0
Slit4	0.39
Slit5	1.53
X-ray camera	2.29
Slit6	10.18

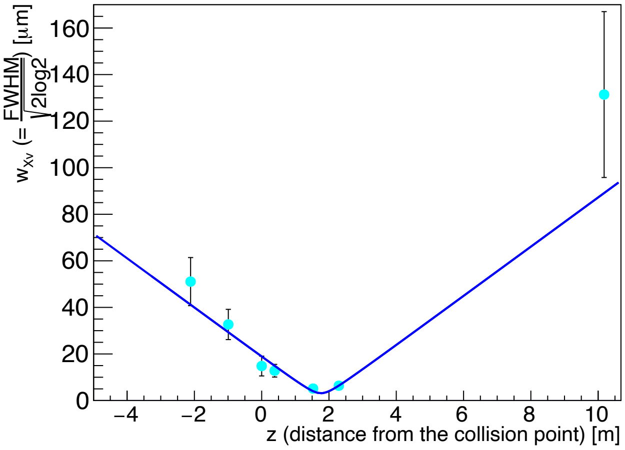

Figure 3.12: The vertical beam size of the XFEL pulse at each position on the beam axis.

3.2 Pump laser system

3.2.1 0.6-TW laser system

The 0.6-TW laser is a Ti:sapphire laser of a 800 nm wavelength [38]. The laser system is composed of a mode-locked oscillator, a chirped-pulse amplifier and a multipass amplifier in the laser hatch (LH). The laser pulse is delivered from LH to the EH2, and its pulse duration is compressed to $\tau_{\mathrm{L}} = 48$ fs (4σ). The intensity of the laser pulse is monitored by a photo diode after the compression. Maximum pulse energy is 3 mJ with 60 Hz. The laser pulse has a gaussian profile of a 7-mm beam size (2σ). The polarization is in the vertical direction, and the angle against the XFEL polarization is $\delta = 90^\circ$. The timing of the laser pulse can be tuned with 6.7 fs step by an optical delay unit that can change the optical path length of the laser pulse.

3.2.2 Optical system

Figure 3.13 shows a whole setup of the optical system. The laser pulse is focused in the chamber. Before the focusing, the laser pulse is expanded by a pair of achromatic lenses. Focal lengths of the Lens3 and the Lens4 are $f = -100$ mm and 250 mm, respectively. The magnification is 2.5.

In the chamber, the laser pulse is focused at the collision point by a 90-degree off-axis parabolic mirror (OAP, Thorlabs, MPD229H-M01) with $f = 50.8$ mm. The OAP has a 3-mm diameter hole on the XFEL beam axis. The hole corresponds to 30 mrad of an angular acceptance from the collision point, which is enough larger than the signal divergence ($\mathcal{O}(10)$ μrad). The OAP is mounted on six-axis stages (three translations and three rotations) to adjust the position and the direction of the laser pulse.

The focal spot is optimized by a deformable mirror (DM, Imagine optic, Mirao 52-e, Fig. 3.14 Right) and a wavefront sensor (WFS, Imagine optic, HASO4 FIRST), which are placed upstream of the OAP. The DM is composed by a silver membrane mirror, and 52 actuators support the back side of the membrane. The membrane mirror has a 17.5-mm diameter of the aperture. The membrane mirror can be deformed and generate an arbitrary aberration by pushed or pulled by the actuators within ±50 μm. Figure 3.14 (Left) shows a system to optimise the focal spot. An aberration of optics is evaluated from the focal spot image. The information on the aberration is fed back to the operation of the DM, and the aberration is canceled. The WFS is used for calibration of the size of the aberration generated by the DM. The WFS is composed of an array of 32×40 microlenses and a CCD sensor. The light passing through the microlenses is focused and makes spots on the CCD sensor. Since the tilt of the wavefront of the laser pulse depends on the positions of these spots, the tilt can be measured from the image of the CCD sensor with a resolution of 5 μrad.

The focal spot of the laser pulse was monitored by the two CCD cameras (Camera1,2 in Fig. 3.13). The Path1 and the Path2 are optical paths for the two cameras, respectively. The Camera1 is used with the Lens5,6, and the Lens5 is the collimation lens. This imaging system has 100 magnifications and is used to measure and optimize the focal spot size. The Camera2 is used with the Lens7,8,9 and Lens10, and the Lens7 is the collimation lens. This imaging system has 7.6 magnifications and is used to measure the focal spot when the XFEL pulse was irradiated. The two imaging systems are switched by inserting or removing a moving mirror and lenses by motorized stages.

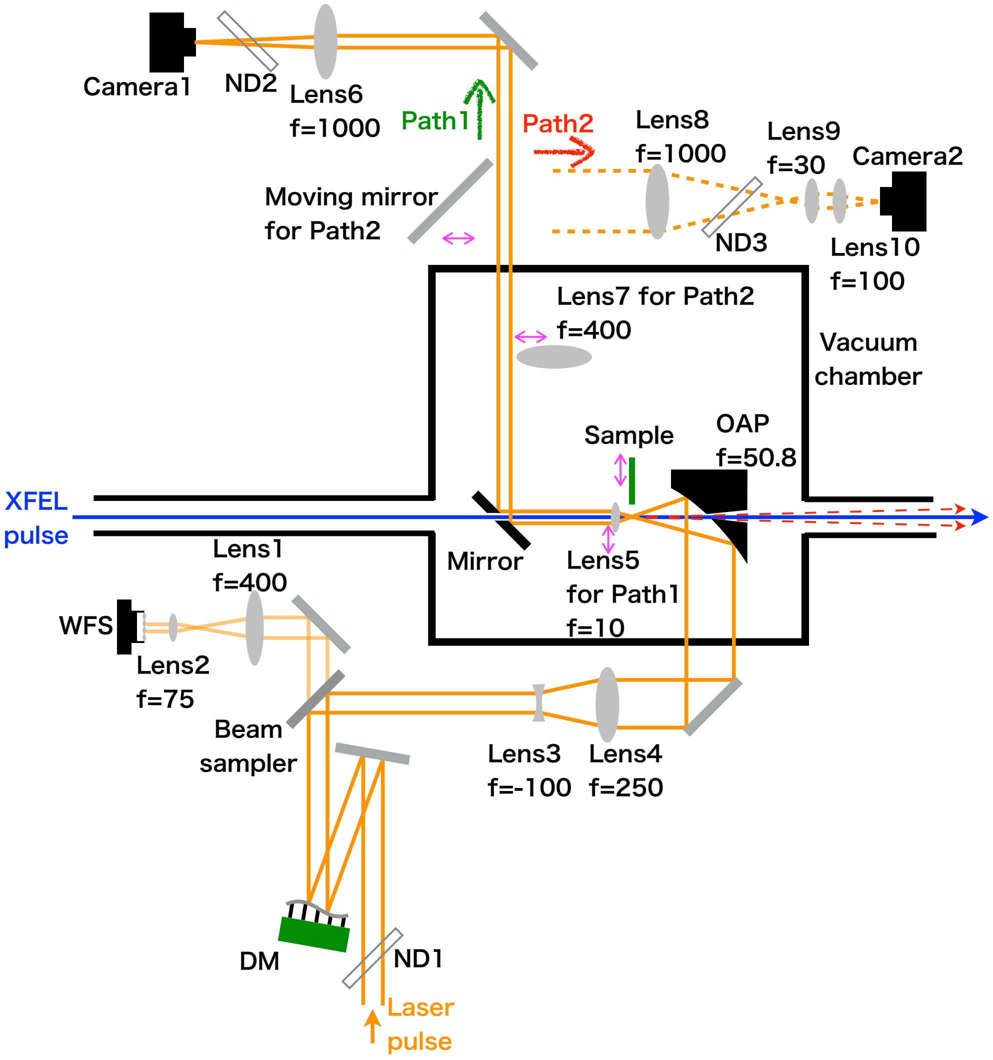

Figure 3.13: A schematic of the whole setup of the optical system. (DM: Deformable mirror with a 17.5-mm diameter aperture; Beam sampler: Beam sampler. 70 % light is reflected and 30 % light goes through.; WFS: Wavefront sensor; OAP: 90 degree off-axis parabolic mirror with a 3-mm diameter hole; Mirror: Plane mirror with a 2-mm diameter hole; Lens1-10: Achromatic doublet lenses; Moving mirror: 76.2-mm diameter mirror for Path2; ND1,ND2 and ND3: Neutral density filter; Camera1 and Camera2: CCD cameras) The collimation lenses (Lens5 and Lens7) and the moving mirror are mounted on the motorized position stage, and can be inserted on the laser beam axis for the two optical paths (Path1 and Path2).

Table 3.3: The summary of optics parameters. (f: Focal length; d: Diameter)

	f [mm]	d [mm]	
Lens1	400	50.8	lens for WFS
Lens2	75	12.7	lens for WFS
Lens3	-100	25.4	lens for expanding the beam size
Lens4	250	50.8	lens for expanding the beam size
OAP	50.8	50.8	focusing optics
Lens5	10	8	lens for Camerea1
Lens6	1000	50.8	lens for Camerea1
Lens7	400	50.8	lens for Camerea2
Lens8	1000	50.8	lens for Camerea2
Lens9	30	30.5	lens for Camerea2
Lens10	100	30.5	lens for Camerea2

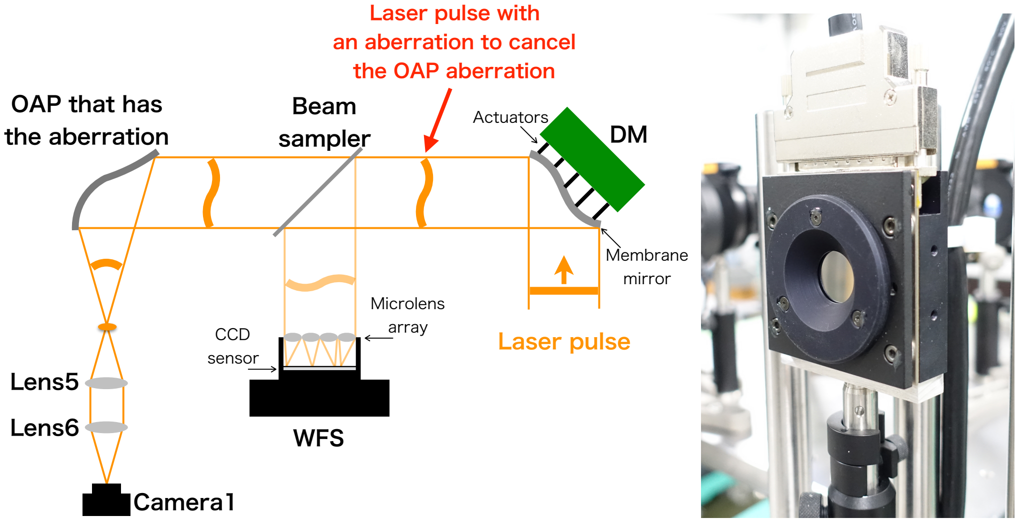

Figure 3.14: A system to cancel an aberration by the DM and the WFS. Left: Schematic of the system. In the figure, the aberration of the OAP is canceled by the aberration generated by the DM. Right: Picture of the DM.

3.2.3 Laser beam and image

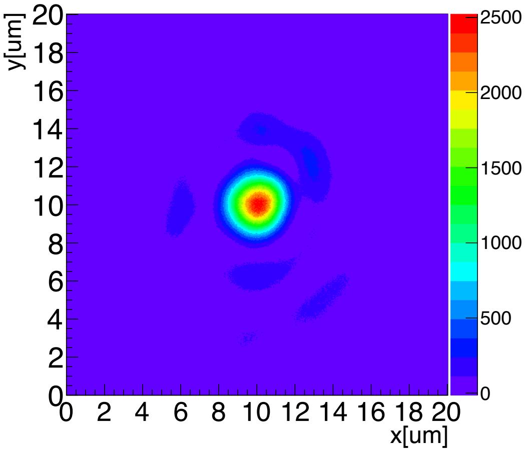

Figure 3.15: The focal spot image of the laser pulse monitored by the Camera1. The horizontal and the vertical sizes are both 1.9 μm (2σ).

The image of the focal spot was measured using the Camera1. Since the Lens5 is thermally damaged if the laser pulse with full pulse energy is irradiated, the pulse energy was reduced using the ND1 during the focal spot measurement. The image with 13% of the full pulse energy is shown in Fig. 3.15. The image was measured with several values of the pulse energy from 10% to 10^{-2}% of the full pulse energy by the ND1. The focal spot was well fitted by two-dimensional gaussian function, and the beam sizes are $w_{\mathrm{L0h}} = 1.9 \pm 0.2$ μm and $w_{\mathrm{L0v}} = 1.9 \pm 0.2$ μm, where dominant uncertainties are the resolution of the imaging system and dependence on the pulse energy.

An effective pulse energy focused in the peak of the image is calculated since a part of the pulse energy is spread over the tail of the peak. The effective pulse energy is evaluated using a total energy in a measured image and an energy in a region of interesting (ROI) with $\pm 2\sigma$ width. The ratio of the effective pulse energy was measured as $a = (30 \pm 3)\%$ against the full pulse energy. The full pulse energy is 1.6 mJ considering a loss by optics, and the effective pulse energy is $W = a \times 1.6$ mJ $= (0.47 \pm 0.06)$ mJ, where a dominant error comes from a dependence of a on the pulse energy.

The beam size and the ratio of concentrated energy around the focus are measured by moving the Lens5. Figure 3.16 shows the horizontal and vertical beam sizes, $w_{\mathrm{Lh}}, w_{\mathrm{Lv}}$. The position, $z = 0$, is corresponding to the image of Fig. 3.15. The horizontal beam size dose not take local minimum due to aberrations of optics. Figure 3.17 is the ratio of the concentrated energy. The ratio becomes large around the focus. In front and back of the focus, the ratio decreases because a part of energy is spread over a tail of the image due to aberrations of optics.

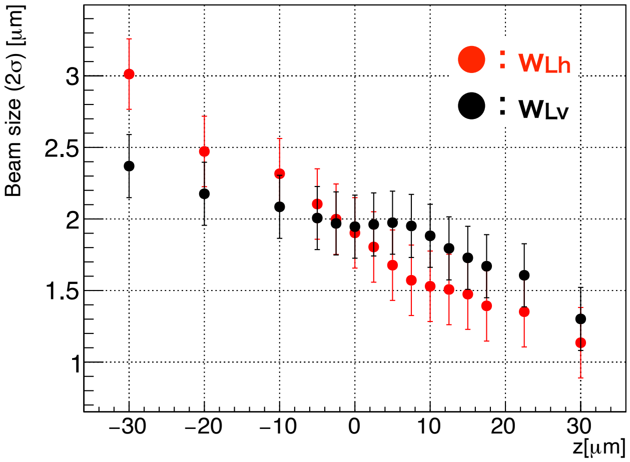

Figure 3.16: Laser beam size. The horizontal and vertical beam sizes, $w_{\mathrm{Lh}}, w_{\mathrm{Lv}}$, are shown with red and black markers, respectively.

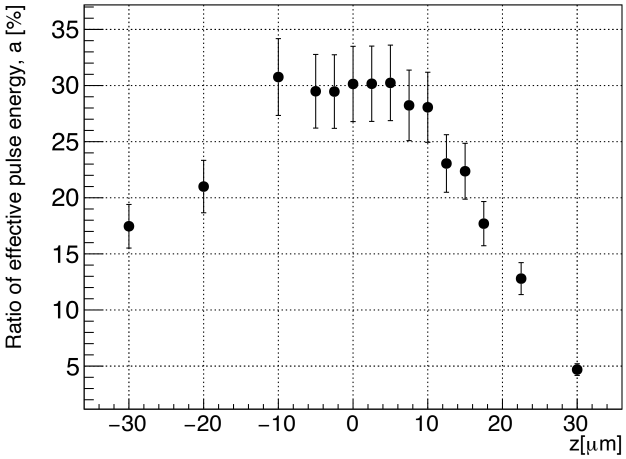

Figure 3.17: Ratio of effective pulse energy concentrated in the spot against the total pulse energy at the collision point.

3.3 Signal detection system

The signal x rays were separated from the probe XFEL pulse by the Slit6 and measured by the PD at EH4c. The vertically diffracted x rays were only selected as the signal. The edges of the blades of the Slit6 and the Slit4 were set upper from the XFEL beam axis. The distance between the XFEL beam axis to the edge of the Slit6 lower blade was $S6_{\mathrm{l}} = (395.0 \pm 3.0)\ \mu\mathrm{m}$ and that of the upper blade was $S6_{\mathrm{u}} = (596.2 \pm 4.4)\ \mu\mathrm{m}$. To block the pass of stray x rays from the XFEL, I use the Slit4 and set the edge of the upper blade at $S4_{\mathrm{u}} = (77.2 \pm 2.2)\ \mu\mathrm{m}$ from the XFEL axis. The uncertainty of these edge positions comes from the accuracy of the measurement of the beam axis position. These positions of the blades correspond to the selection angles of $\theta_y < 200\ \mu\mathrm{rad}$ with the Slit4 and $39 < \theta_y < 59\ \mu\mathrm{rad}$ with the Slit6.

Figure 3.18 shows a image of the PD (HAMAMATSU, S3590-09). The PD is the equipment of the XFEL beamline, and placed in the vacuum pipe of the beamline. The PD has 10 mm×10 mm aperture and 300 μm-thick depletion layer. An energy resolution is measured by simultaneous measurement of XFEL pulse with the SCM, and the energy resolution is 2.8%. A detection efficiency for 8.4 keV x-ray is evaluated with a Monte Carlo simulation using Geant4 as $(97.8 \pm 0.8)\%$.

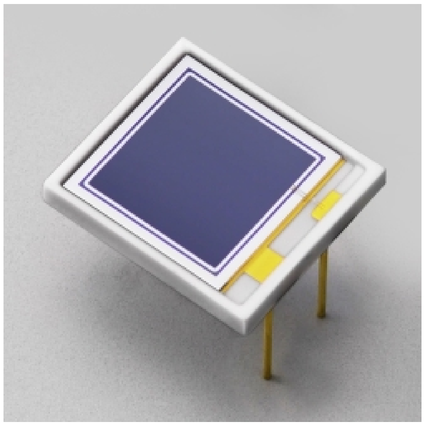

Figure 3.18: Image of PD (HAMAMATSU, S3590-09, [39]).

Chapter 4

Alignment of two beams

4.1 Spacial alignment

The position of the laser pulse is adjusted to make both pulses collide head-on. The positions of the laser pulse and the XFEL pulse are measured using the Au foil. The spacial alignment has been performed by iterating the adjustment of the laser position and the measurement of both pulse positions. The adjustment of the laser position is summarized in Sec. 4.1.1, and measurements of the position of both pulses are summarized in Sec. 4.1.2 and Sec. 4.1.3, and the result of the spatial alignment is shown in Sec. 4.1.4.

4.1.1 Adjustment of the laser position

The position of the laser pulse is adjusted using the six-axis stages on which the OAP is mounted. The position and the direction of the laser pulse were adjusted with 0.25 μm or about 10 μrad step using the stages.

After the adjustment, the displacement between both pulses was measured using the Au foil set around the laser focus. Both pulses were irradiated to the 30-μm-thick Au foil mounted on the sample folder (Fig. 3.7). The displacement was measured from the position of the irradiation trace of both pulses. Figure. 4.1 shows the image of the irradiation traces. The irradiation trace of the XFEL pulse is a hole shown at the top in the figure. Totally 150 XFEL pulses were irradiated. The irradiation trace of the laser pulse is a crater shown at the bottom in the figure. One laser pulse was irradiated. In order to avoid overlapping of both traces, the Au foil was moved upward by 100 μm after the irradiation of the XFEL pulse.

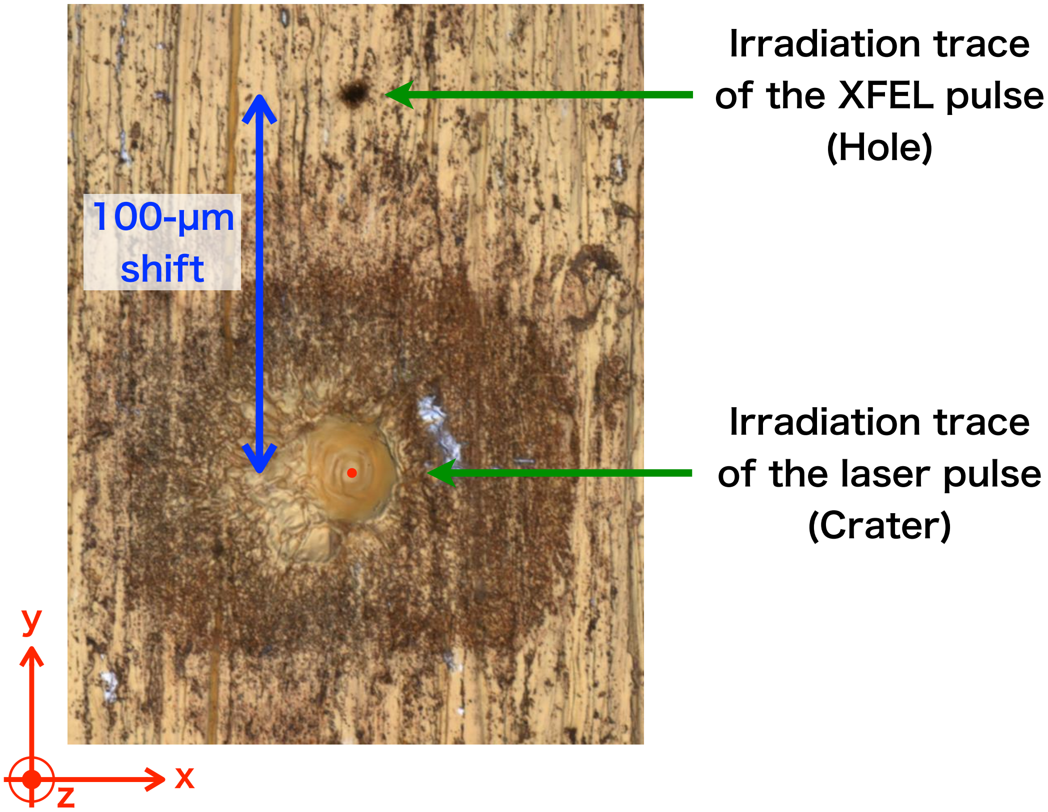

Figure 4.1: The microscope image of the irradiation traces of the laser pulse and the XFEL pulse on the Au foil. The top hole is the irradiation trace of the XFEL pulse (150 pulses), and the bottom crater is that of the laser pulse (1 pulse), To avoid the overlap between the two traces, I shifted the Au foil by 100 μm in a transverse direction against the beam axis after the irradiation of the XFEL pulses. A red dot shows the estimated center position of the crater.

The coaxiality of two beams is also measured by measuring the displacement at two positions along the beam axis.

After taking the Au foil from the chamber, the irradiation traces were measured by a laser microscope (Olympus, OLS4100). The laser microscope can measure a black-and-white or a three-dimensional image with 405 nm light.

4.1.2 Measurement of laser position

When a laser pulse is irradiated to the Au foil, a high-pressure vapour of plasma is generated by Au atoms on the surface of the foil. This high-pressure vapour becomes a shock wave and creates the irradiation traces like a crater on the foil. Thus, the center of the laser pulse corresponds to the deepest position of the crater.

The deepest position of the crater is observed by the three-dimensional image

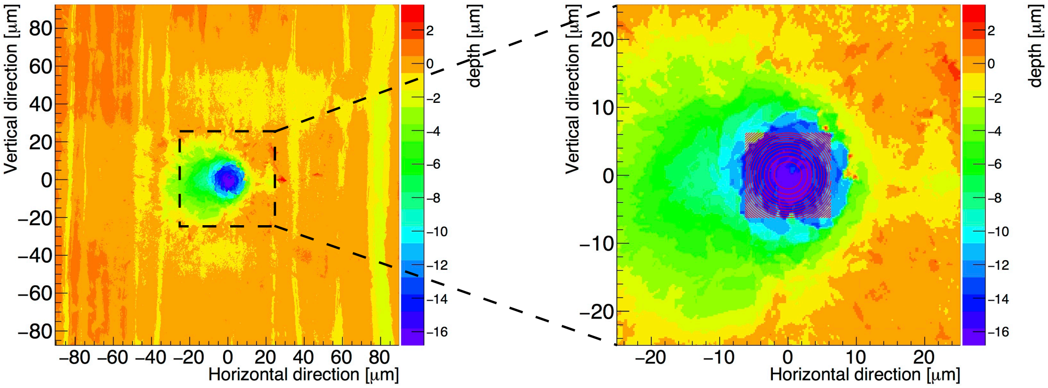

Figure 4.2: The height profile of the crater of the laser irradiation traces. The profile is fitted by paraboloid function (red line).

measured by the laser microscope. The image is shown in Fig. 4.2. The deepest position is measured by fitting the ROI in the image with a paraboloid function. The size of the square ROI is changed from 8 μm to 18 μm. The uncertainty of the deepest position due to a fitting error is ± 0.04 μm and that due to a dependence on the ROI size is ± 0.5 μm.

Since each crater shape around the deepest position is slightly different, the stability of the deepest position against the crater shape is investigated. Figure 4.3 is a height profile of the crater taken by projecting the three-dimensional image with 13 μm width. The origin is the bottom of the fitted paraboloid function. Each point shows an average of the profile of the six crater data (shown in Sec. 4.1.4). Each profile is normalized by a depth of the crater before the averaging to compare the shape of the profile. An error bar shows root mean square (RMS) of a fluctuation of the height of each profile. The shape of the profile is very stable. An intensity profile of the laser pulse, which is the projection of the two-dimensional intensity profile, is also shown as a green line for the comparison. The center position of the two-dimensional intensity profile corresponds to the origin of the graph. Although the profile in the horizontal direction is asymmetry due to a tail of the laser profile, the shape of the crater is stable as well as the vertical profile. Figure 4.4 is a closed view of Fig. 4.3 around the deepest position. Due to the instability of the shape, the deepest position has the uncertainty of 1.4 μm and 2.3 μm in horizontally and vertically. Summarizing all the uncertainties, a total accuracy of the laser position measurement is a quadratic sum of all uncertainties and is ± 1.5 μm and ± 2.4 μm horizontally and vertically, respectively.

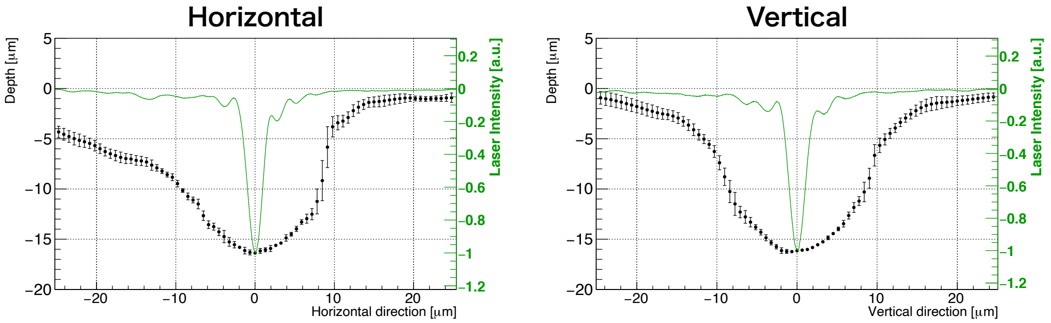

Figure 4.3: Height profile of the crater. For a comparison, a laser intensity profile is also shown with a green line. Left: in the horizontal direction. Right: in the vertical direction.

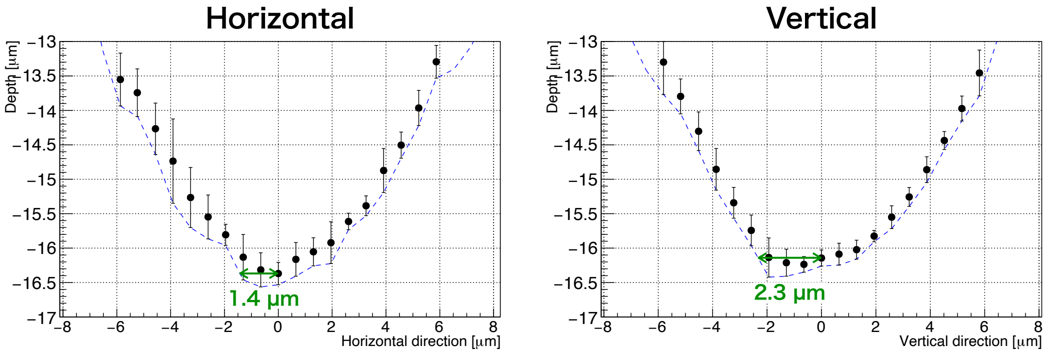

Figure 4.4: Closed view of Fig. 4.3. Left: in the horizontal direction. Right: in the vertical direction.

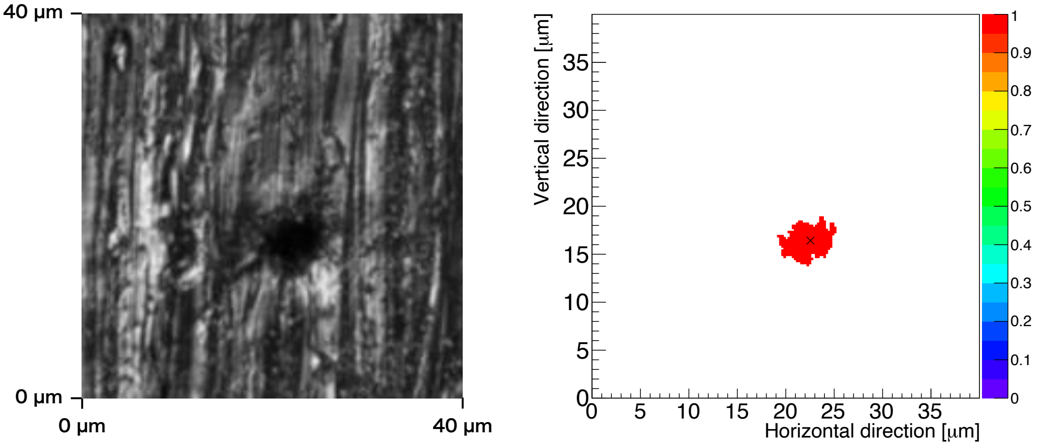

Figure 4.5: The image of the hole of the XFEL irradiation traces. Left: The black-and-white image of the hole taken by the laser microscope with 405 nm light. Right: The binarized image. The threshold of the brightness for the binarization is 15% to 35% against the maximum brightness in the black-and-white image. The 25% case is shown. The black cross marker shows the center of the hole.

4.1.3 Measurement of XFEL position

When the XFEL pulse is irradiated to the Au foil, Au atoms on the surface are vaporized as well as the laser irradiation. Since the intensity of the XFEL pulse ($\sim \mu$J) is smaller than that of the laser pulse ($\sim$mJ), an influence of the shock wave is weak, and a crater is not created. Instead of a crater, a through hole is created by repeating the irradiation and the vaporization. Since the hole is created depending on the x-ray intensity, the center of the hole is estimated as the peak position in the XFEL profile.

The center of the hole is observed by a black-and-white image measured by the laser microscope. Figure 4.5 left shows the image. The region of the hole is dark since lights of the laser microscope, which illuminate the foil, are not reflected by the hole. The brightness of the image is binarized to observe the shape of the hole. Figure 4.5 right is the binarized image. Figure 4.6 is the projection of the binarized image, and the red line shows the FWHM of the histogram, which is a width of the hole. The centers of the FWHM shown with black crosses are estimated as the peak positions of the horizontal and the vertical XFEL profiles. Considering that the peak position of the XFEL profile is certainly in the region of the hole, the uncertainty of the peak position is calculated as FWHM/$\sqrt{12}$. Three data of the holes (shown in Sec. 4.1.4) are evaluated, and averages of the FWHM are 3.5 μm and 2.9 μm in the horizontal and the vertical directions, respectively. From these, the uncertainties of the peak positions are ± 1.0 μm and ± 0.9 μm in the horizontal and the vertical directions, respectively. Dependence of the peak position on the threshold of the brightness for the binarization is also evaluated. The dependences

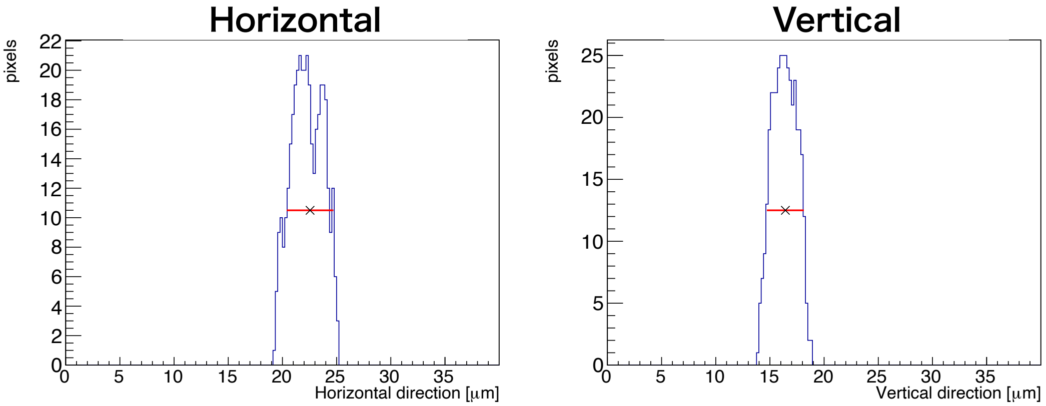

Figure 4.6: The projections of the binarized image of the hole (Fig. 4.5 right) shown by the blue histogram. The red line shows the FWHM of the histogram. The black cross marker shows the center of the hole, which is the center of the FWHM. Left: The projection to the horizontal direction. Right: The projection to the vertical direction.

are ±0.3 μm and ±0.1 μm in the horizontal and the vertical directions, respectively.

The XFEL position ($x = y = 0$ in the profile of Fig. 3.11) is calculated by considering a gap from the XFEL position to the peak position of the XFEL profile. The gaps are (2.2 ± 3.1) μm and (3.4 ± 1.7) μm in the horizontal and the vertical directions, and these uncertainties of the gap are mainly caused by the interval of the knife-edge scan for the XFEL profile measurement. Summarizing all uncertainties, the accuracies of the XFEL position measurement are ±3.3 μm and ±1.9 μm in the horizontal and the vertical directions, respectively.

4.1.4 Result of spacial alignment

After a few iterations of the adjustments and the displacement measurement, the displacement was measured. Data of the irradiation traces were taken six times, and the images of the traces are shown in Fig. 4.7. The hole was created only three times out of six times of the x-ray irradiation due to the fluctuation of the pulse energy. Figure. 4.8 shows the measured position of each pulse. Blue and Orange markers show the XFEL position and the laser position, respectively. An average of the XFEL position is taken as the origin. The distance of the horizontal or vertical shift to avoid the overlap of the irradiation trace is corrected in the calculation. From the average of the laser positions, the displacements are calculated as $x_{\mathrm{L}} = 0.7$ μm and $y_{\mathrm{L}} = 4.8$ μm. From the fluctuation of the measured positions, the fluctuation of both pulses is evaluated as about 0.4 μm.

The coaxiality is also measured. The foil position was moved ±25 μm, and at each foil position, the position of pulses was measured. The angle between both axes of beams was (0 ± 67) mrad. If there is a small angle between both axes, the

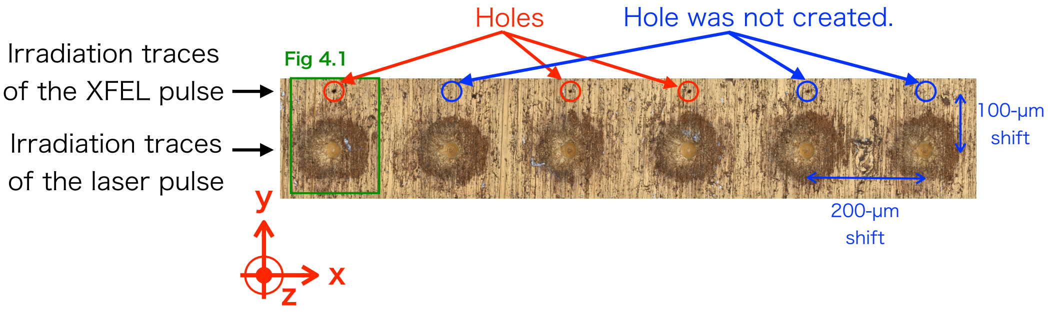

Figure 4.7: The image of the irradiation traces on the Au foil. The area surrounded by a green rectangle is Fig. 4.1.

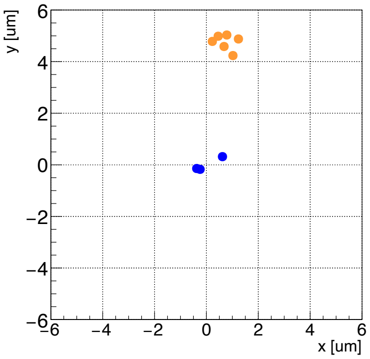

Figure 4.8: The distributions of the XFEL positions (blue) and the laser positions (orange) against the averaged XFEL position. The averaged position of the XFEL pulse is set to be the origin ($x = y = 0$).

displacement changes along the z-direction. The laser size was measured in the region of $z = \pm 30\ \mu$m. The uncertainty of the displacement due to the coaxiality uncertainty is $\pm 30\ \mu\text{m} \times 67\ \text{mrad} = \pm 2.0\ \mu$m.

The total uncertainties of the displacement are calculated by the quadratic sum of all uncertainty, and are $\pm 4.2\ \mu$m and $\pm 3.7\ \mu$m, in the horizontal and the vertical directions, respectively. The uncertainties are summarized in Tab 4.1.

Table 4.1: The summary of the uncertainties of the horizontal displacement, x_{L}, and the vertical displacement, y_{L}.

Sources of uncertainty	Uncertainties of x_{L} [μm]	Uncertainties of y_{L} [μm]
Measurement of the XFEL position	3.3	1.9
Measurement of the laser position	1.5	2.4
Fluctuation of the XFEL position	0.3	0.5
Fluctuation of the laser position	0.4	0.3
Uncertainty of coaxiallity	2.0	2.0
Total uncertainty of the displacement	4.2	3.7

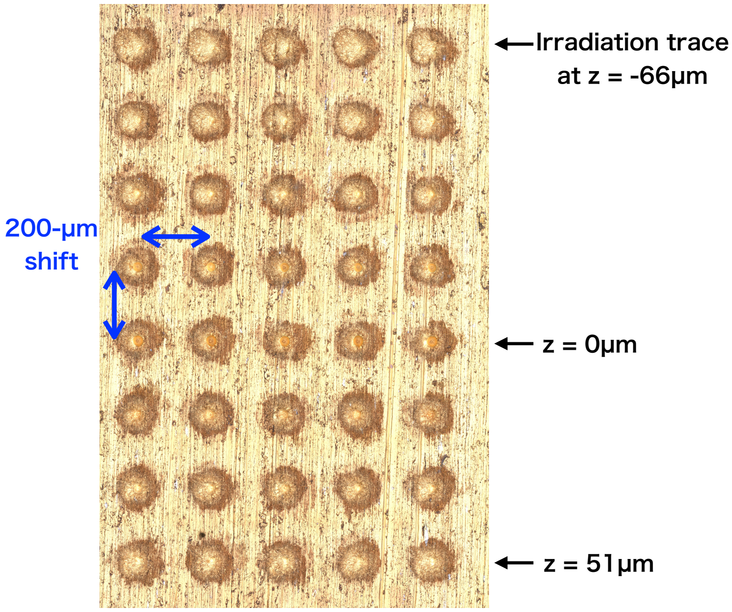

Figure 4.9: Irradiation traces of the laser pulse. The foil is moved about ±60 μm along the beam axis, and the laser pulse is irradiated five times at each foil position.

4.2 Time alignment

To collide both pulses when the laser pulse is focused, the delay time of the laser pulse is adjusted. The focal position of the laser is measured using the Au foil. A timing when both pulses are collided at the focus is measured using the GaAs crystal set at the focus. The accuracy of the time alignment is determined by this measurement.

4.2.1 Measurement of the focal position of the laser

The focal position of the laser in the z-direction is measured using the information of the depth of the irradiation trace since a focused laser creates a deep crater. Figure 4.9 shows the created craters on the Au foil. The laser pulse was irradiated five times, and the foil was moved by about ±60 μm in the z-direction. In order to avoid the overlap of craters, the foil was transversely shifted 200 μm against the z-axis after the irradiation.

The depth of the craters is measured by the three-dimensional image of the laser microscope, and the average of the depth at each position of the foil is shown in Fig. 4.10. The vertical error shows a fluctuation of the depth, and the horizontal error is mainly caused by a warp of the foil. The deepest position in Fig. 4.10 ($z = 0$ μm) is estimated as the focal position, and the uncertainty corresponds to 17 μm of the interval between points, which is shown by a green arrow.

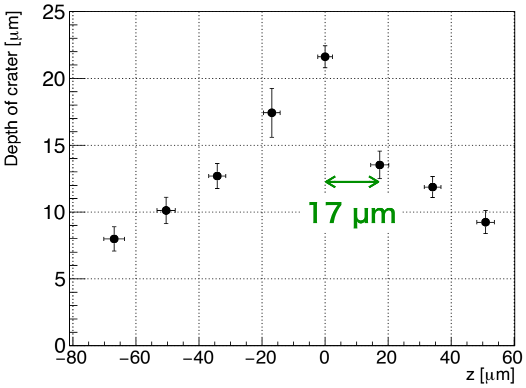

Figure 4.10: Depth of irradiation traces of the laser pulse at each position along the beam axis.

4.2.2 Adjustment of the delay time of the laser

The delay time of the laser is adjusted in a two-phased approach. First, both pulses are detected by a photodiode set around the focal position, and a time to oscillate the laser pulse is adjusted. By this adjustment, a difference of timings when both pulses arrive becomes within ~ 100 ps.

Next, the delay time of the laser is adjusted using a GaAs crystal. A GaAs crystal irradiated by x rays is ionized and becomes opaque against the laser lights [36,37]. Since this process is very fast (< 0.1 ps), using this process, the delay time of the laser can be adjusted to about 0.1 ps accuracy. The used GaAs crystal is shown in Fig. 3.7. The 5-μm-thick GaAs crystal glued on a 500-μm-thick sapphire substrate is placed around the focal position and irradiated by the XFEL pulse. The laser pulse is also irradiated, and transmittance is monitored by the Camera2. The delay time of the laser was adjusted by the optical delay unit with a 6.7 fs step. Fig. 4.11 is the image detected by the Camera2. In the left (right) image of Fig. 4.11, the laser pulse was irradiated earlier (later) than the XFEL pulse. In the right image, the transmittance of the laser is decreased. By detecting this phenomenon, the difference of timings of both pulses is adjusted within about 0.1 ps.

4.2.3 Precise measurement of the collision timing

Measurement of the collision timing

After the adjustment of the delay time, a collision timing when both pulses collide at the focal position ($t_{\mathrm{L}} = 0$) was measured by the transmittance of the laser. The surface of the GaAs crystal was placed at the focal position as shown in Fig. 4.12 (Left), and the transmittance of the laser was measured against the delay time. If the duration of both pulses and a time of the optical response of GaAs against the x rays irradiation are very short, the transmittance of the laser decrease

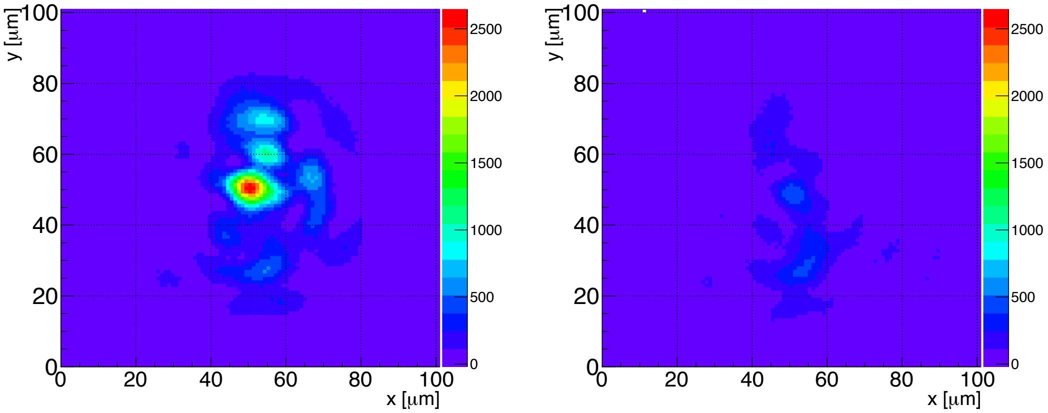

Figure 4.11: The image of the laser through the GaAs crystal detected by the Camera2. The image is distorted by the GaAs crystal and the substrate. Left: The laser pulse was irradiated to the GaAs crystal earlier than the XFEL pulse. Right: The laser pulse was irradiated to the GaAs crystal later than the XFEL pulse. The irradiation of the XFEL pulse makes the GaAs opaque against the laser lights, and the transmittance of the laser lights is decreased.

as shown in Fig. 4.12 (Right). When t_L is 0, the transmittance gets down. The width of the slope (0.08 ps) corresponds to the sum of a time when the laser pulse passes through the GaAs crystal and a time when the XFEL pulse passes through.

Figure 4.13 shows the pulse-by-pulse distribution of the laser transmittance versus the delay time. The delay time was scanned around the timing when the transmittance decreases. Since there is the jitter (~ 0.3 ps), the delay time of each laser pulse is calculated using the TM. The transmittance is calculated using the energy in the square ROI whose center is the peak of the image (Fig. 4.11 (Right)). The analysis is evaluated with the size of the square ROI from 6 μm to 65 μm, and the result with a 35 μm case is shown in Fig. 4.13. The timing when the transmittance gets down, t_0, is observed by the fitting the transmittance by following function

$$f(t_\mathrm{L}) = \begin{cases} 1 & (t_\mathrm{L} < t_0) \\ 1 - b(t_\mathrm{L} - t_0) & (t_0 \le t_\mathrm{L}) \end{cases} \tag{4.1}$$

where b is a constant. Since the collision timing ($t_\mathrm{L} = 0$) agrees with the timing when the transmittance gets down (t_0), t_0 is 0.

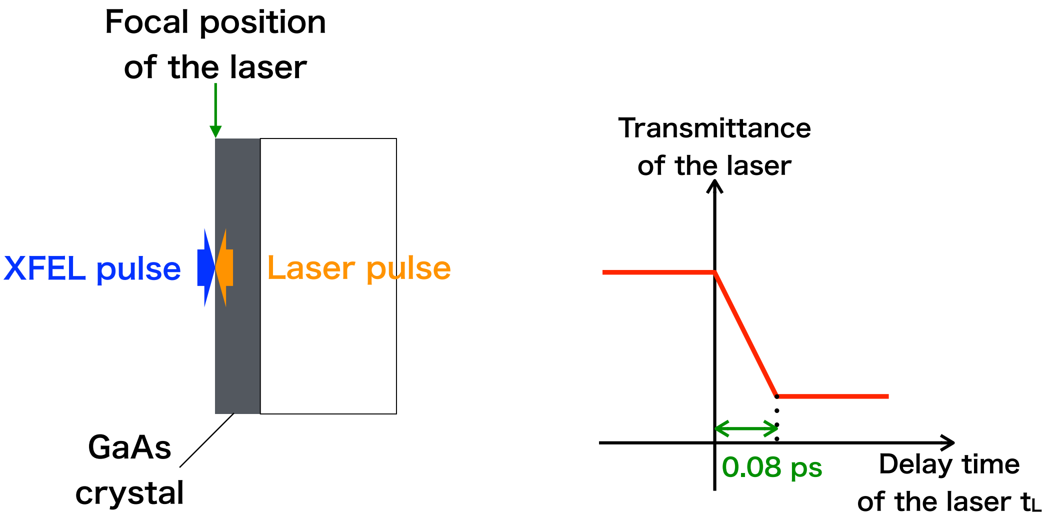

Figure 4.12: Left: Schematic of the GaAs crystal and both pulses at the collision timing. Right: Laser transmittance versus delay time in the ideal situation. The durations of both pulses and the optical response of the GaAs are assumed to be very short ($\ll 1$ fs).

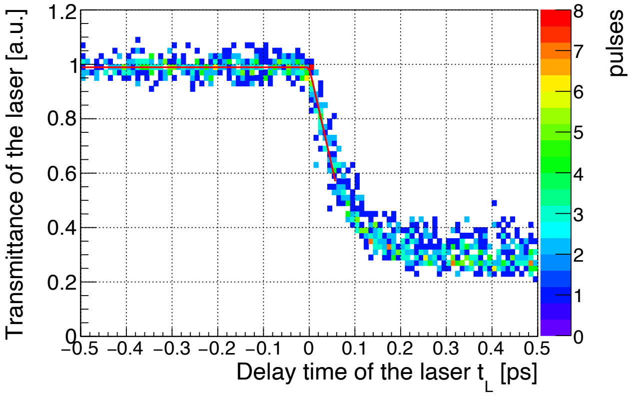

Figure 4.13: The pulse-by-pulse distributions of the laser transmittance of the GaAs crystal. The horizontal axis is the delay time of the laser. Since the irradiation of x rays makes the GaAs opaque against the laser lights, the transmittance becomes less than 1 in the region $t_L > 0$.

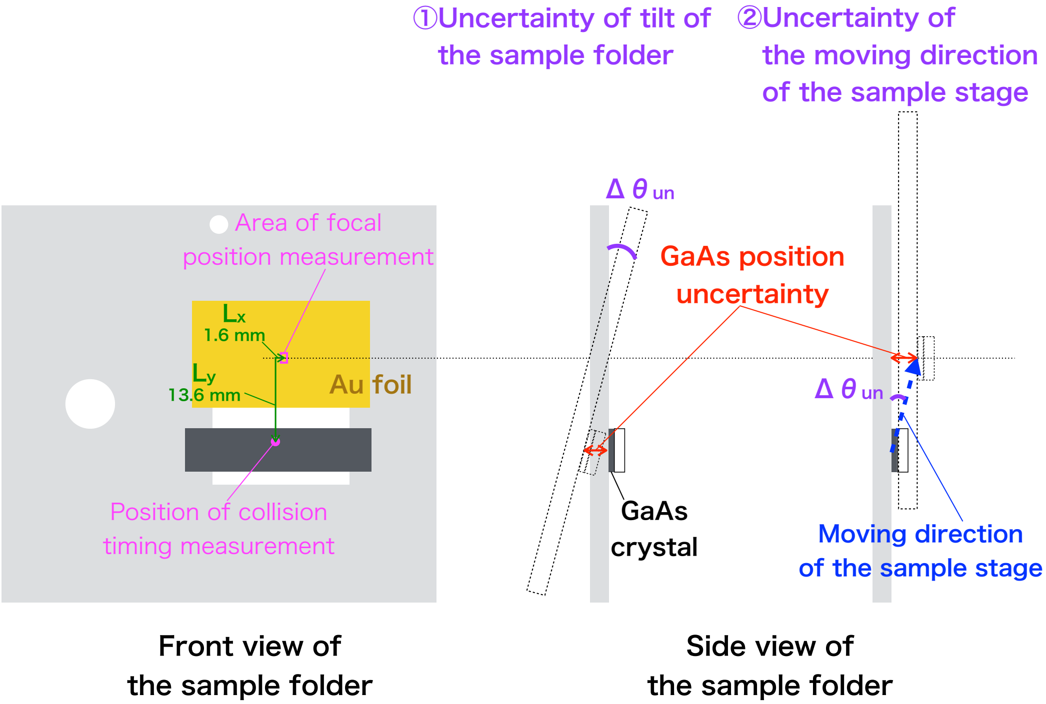

Figure 4.14: Two kind of sources of GaAs position uncertainty in the beam axis direction. The schematic of the sample folder is shown with the front view and the side view. One of the sources is the uncertainty of the tilt of the sample folder (middle schematic). The other is the uncertainty of the moving direction of the sample stage (right schematic).

Uncertainty of the collision timing

Large uncertainties of the collision timing measurement are caused due to the analysis and misalignment of the GaAs crystal. In the analysis, dependencies of the collision timing on the ROI size and the fit width are evaluated. The uncertainties due to these dependencies are 20 fs and 18 fs, respectively. Due to the finite pulse duration, the edge in the ideal transmittance graph (at $t_{\mathrm{L}} = 0$ in Fig. 4.12) is rounded. The uncertainty due to this effect is 28 fs.

Other sources of uncertainties are the misalignment of the GaAs crystal in the beam direction. Figure 4.14 shows a schematic of the sample folder and sources of the GaAs position uncertainty. The tilts of the sample folder and the moving directions of the sample stages have an uncertainty, $\Delta\theta_{\mathrm{un}}$, as shown in the middle and the right of Fig. 4.14. The tilt uncertainties of the sample folder were ±0.3 mrad and ±0.7 mrad in the horizontal and the vertical direction, respectively. The moving direction uncertainties of the sample stage were ±2.1 mrad and ±0.9 mrad. On the sample folder, the distances from the position of the collision timing measurement to the position of the focal point measurement are horizontally $L_x = 1.6$ mm

Table 4.2: The summary of the temporal uncertainties of the collision timing.

Sources of uncertainty	GaAs position uncertainty [μm]	Temporal uncertainty [fs]
ROI dependence of t_0	-	20
Fit width dependence of t_0	-	18
Pulse width of both pulses	-	28
Resolution of TM	-	6
Thickness of the sapphire substrate	-	6
Horizontal tilt of the sample folder	0.4	3
Vertical tilt of the sample folder	9	62
Horizontal tilt of the stage moving direction	3	22
Vertical tilt of the stage moving direction	12	79
Focal position measurement	17	118
Total temporal uncertainty		160

and vertically $L_y = 13.6$ mm. Due to the distance, the position of the GaAs crystal during the collision timing measurement has uncertainty as $\pm L_x \times \tan(\theta_{\mathrm{un}})$ or $\pm L_y \times \tan(\theta_{\mathrm{un}})$, as shown in Fig 4.14. The maximum of these uncertainties is $\pm 12\mu$m.

The uncertainty of the focal position measurement, 17 μm, also causes the uncertainty of the GaAs crystal position.

All uncertainties are summarized in Tab. 4.2. The uncertainty of the collision timing in total becomes the quadratic sum of those and was ±160 fs.

Result and accuracy of the time alignment

The delay time of measured data in the VD search has a width of about 0.3 ps due to the jitter of both pulses. Since the delay time is precisely measured by the TM, the accuracy of the time alignment is determined by the accuracy of the collision timing measurement. Thus, the accuracy of the time alignment is ±160 fs.

Chapter 5

Data taking and analysis

5.1 Data taking

5.1.1 Data acquisition of vacuum diffraction

Table 5.1: The summary of the data acquisition of vacuum diffraction. The collision data and the BG data were measured alternately with the conditions summarized in the table.

	Wide range scan	Narrow range scan
Range of the scan	6.9 ps	2.9 ps
Number of steps for the scan	27	12
Interval between steps	267 fs	267 fs
Statistics of data in one step	15	150
Repetition of scan	5	5

The VD search was performed for about 20 minutes on July 1, 2019. Both pulses were collided, and diffracted x rays were searched. During the data acquisition, the delay time of the laser was scanned using the optical delay unit. The delay time was scanned with a wide range (6.9 ps) and a narrow range (2.9 ps), and each range was scanned with 267 fs of the interval. The scan with the wide range was performed to confirm a stability of BG amount in the timing distribution of the delay time. The scan with the narrow range was performed to take a lot of data when both pulses are collided at the focus of the laser. These scans were repeated five times. Conditions of the scans are summarized in Tab. 5.1 and Fig. 5.1. Two kinds of data were taken. One is a collision data when both pulses are collided, and the other is a BG data when only XFEL pulse is irradiated. Both data were measured alternately using the 30 Hz of the XFEL pulse, and both data were obtained at 15 Hz. One BG data observed after one collision data is used as BG of its collision

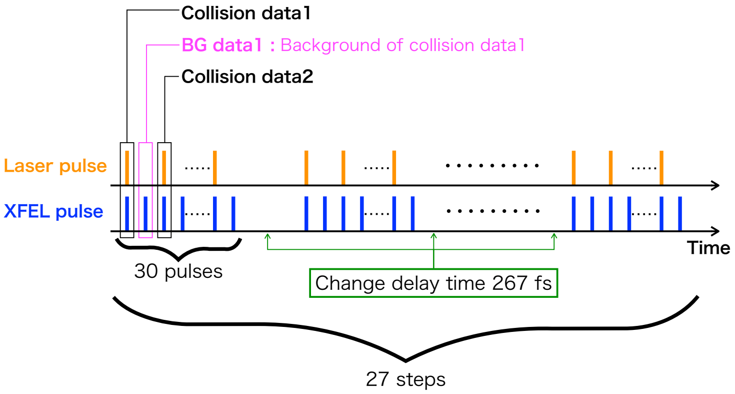

Figure 5.1: Illustration of the way of the scan of the delay time with the wide range (6.9 ps). During the data acquisition, the wide range scan was repeated five times, and after that, the narrow range scan was also repeated five times.

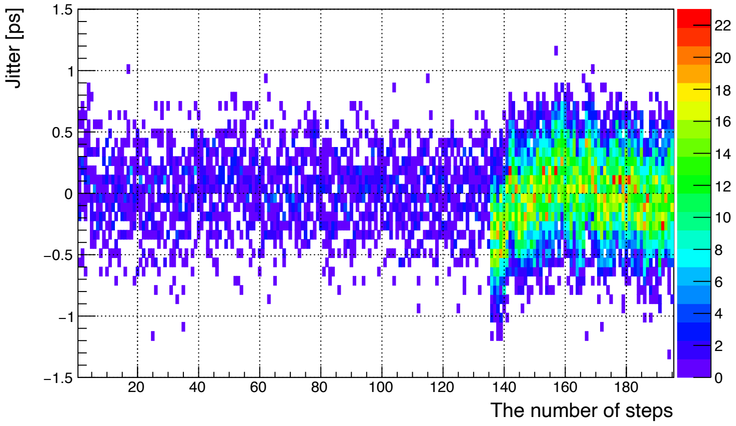

Figure 5.2: The jitter of each pulse during the data acquisition.

data. In total, 11025 pulses of both data were taken, respectively. The x rays through the openings of the slits were measured and recorded for every pulse.

Figure 5.2 shows the jitter of the collision data of each pulse. The horizontal axis shows each step of the scans, and the first 135 steps correspond to the scan with the wide range. The vertical axis is the jitter, which is a delay time of the oscillation timing of the laser against the XFEL. The jitter shows a gaussian-like distribution with the RMS of about 300 fs. Though the median of the jitter at each step has a slight drift ($\sim$ 10 fs/step) during the scans, the drift is enough smaller than the jitter size and the delay time added at each step.

Figure 5.3 shows the timing distribution of all collision data. The horizontal axis shows the delay time of the laser. The timing distribution has finer structures than the interval of the scan (267 fs) due to the jitter.

Figure 5.4 is the number of photons in the XFEL pulse for each step. The

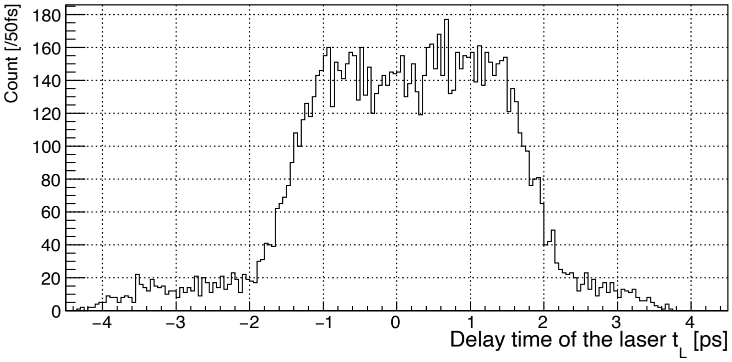

Figure 5.3: The timing distribution of the collision data. The horizontal axis shows the delay time of the laser. The vertical axis shows counts of the collision.

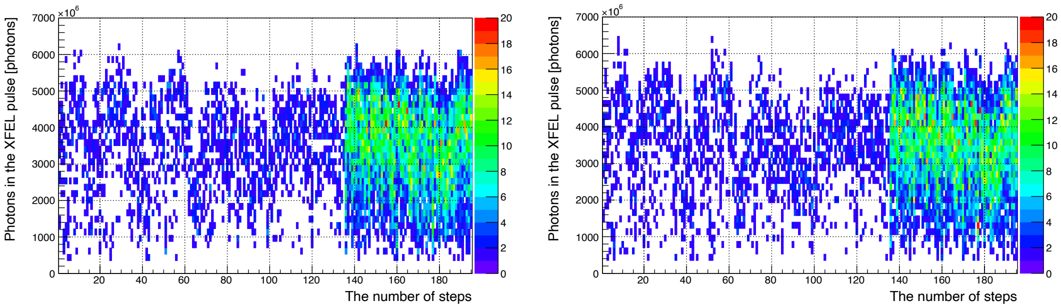

Figure 5.4: The number of photons in the XFEL pulse during the data acquisition. Left: The collision data; Right: The BG data.

photons of each pulse are shown and have about 30% of the intensity fluctuation (RMS) at each step. Figure 5.5 shows a magnified view of the timing distribution of photons in the XFEL pulse. Each bin shows the average number of photons in the XFEL pulse at the collision point. Black and magenta points show the collision data and the BG data, respectively. A timing window for the analysis is the area between green lines. In the analysis, the signal is calculated in the region where the beam size of the laser was measured. This region is $|z| \leq 30\ \mu$m, which corresponds to $|t_{\mathrm{L}}| < 0.2$ ps. The timing window is determined to be $|t_{\mathrm{L}}| < 0.55$ ps, which contains the region of the signal (± 0.2 ps) with the accuracy of 2σ (± 0.32 ps, 2σ of the time alignment accuracy). The number of photons of the collision data in the timing window was $N = (3.46 \pm 0.02) \times 10^9$ photons/pulse on average.

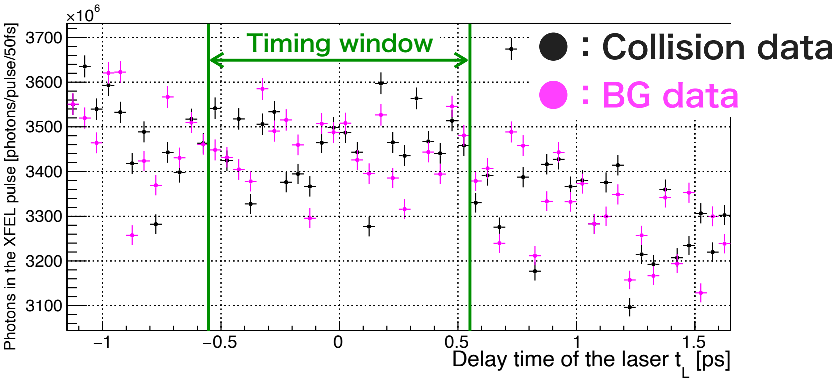

Figure 5.5: The timing distribution of the number of photons in the XFEL pulse at the collision point. The collision data and the BG data are shown with black and magenta points, respectively.

5.1.2 Monitoring of position drift of both pulses

The images of both pulses are measured by the Camera2 to monitor the drift of the positions of both pulses. Figure 5.6 shows the images of both pulses. The image of the laser pulse has a diffraction pattern around its peak since the aperture of the Lens7 (ϕ46 mm) is smaller than the laser pulse at the Lens7 ($\sim \phi$60 mm). Different from the image of the laser pulse, the image of the XFEL pulse was measured using the GaAs crystal. A GaAs emits fluorescence after absorption of the x rays. The XFEL pulse was irradiated to the GaAs crystal set at the focus of the laser, and the image of fluorescence was measured.

In my research, the position of the laser pulse was drifted due to a slight movement of the chamber. In this situation, the laser image on the picture does not move since the laser pulse moves together with the imaging lens (Lens7). In contrast, the XFEL image moves inversely with the Lens7.

The drift of both pulses was measured by tracing the peak of the images before and during the data acquisition. Figure 5.7 shows the drift of the peaks of both images. The average of the peak position with 150 pulses is shown with its error due to the fluctuation. The orange and the blue points are the peaks of the laser and the XFEL, respectively. The horizontal axis, T, is a time from the start of the data acquisition. The peak of the XFEL image changes due to the drift of the laser pulse. In order to estimate this drift, the peak of the XFEL image is fit by a blue linear function. This function corresponds to the drift of the laser pulse, and a light blue hatch is its uncertainty due to the fluctuation, which is a maximum gap from this function to the blue points (horizontally 0.6 μm and vertically 0.8 μm). In order to cancel the displacement due to the drift, the laser pulse was vertically shifted by 4.25 μm by the OAP stage before the data acquisition.

The displacement between both pulses after the spatial alignment is calculated by comparing the peak of the laser and the linear function in Fig. 5.7, and the

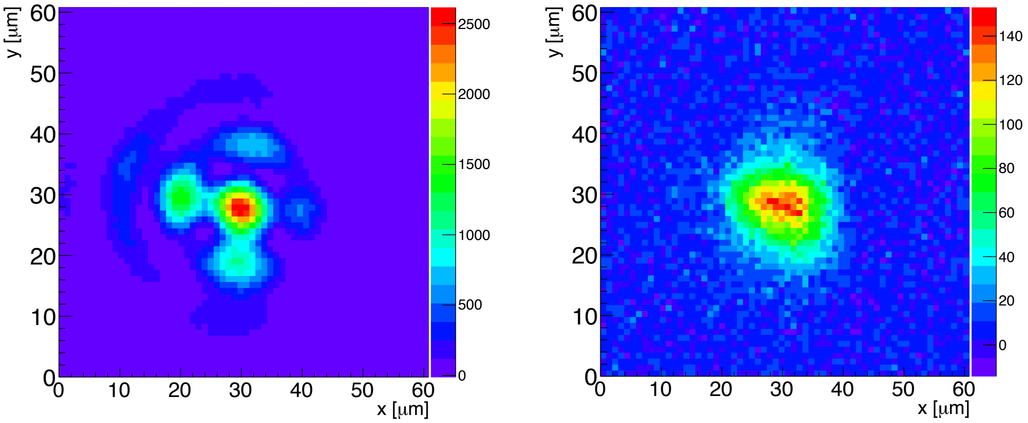

Figure 5.6: Images of the laser pulse and the XFEL pulse measured by the Camera2. Left: Image of the laser focal spot; Right: Image of the fluorescence of the GaAs crystal which is irradiated by the XFEL pulse.

result is shown in Fig 5.8. A time when the spatial alignment has been performed ($T = -1.4$ hour) is shown with the red line. The green hatched area is the duration of the data acquisition, and the displacements at first 150 pulses of the ten delay time scans and end 150 pulses of the last delay time scan are shown. Displacements during the data acquisition, which is the average of displacements in the green hatch area, are $x_{\mathrm{L}} = (0.5 \pm 4.2)$ μm and $y_{\mathrm{L}} = (2.9 \pm 3.8)$ μm, where each error is a quadratic sum of the spatial alignment uncertainty and the fluctuation of the position drift of the chamber.

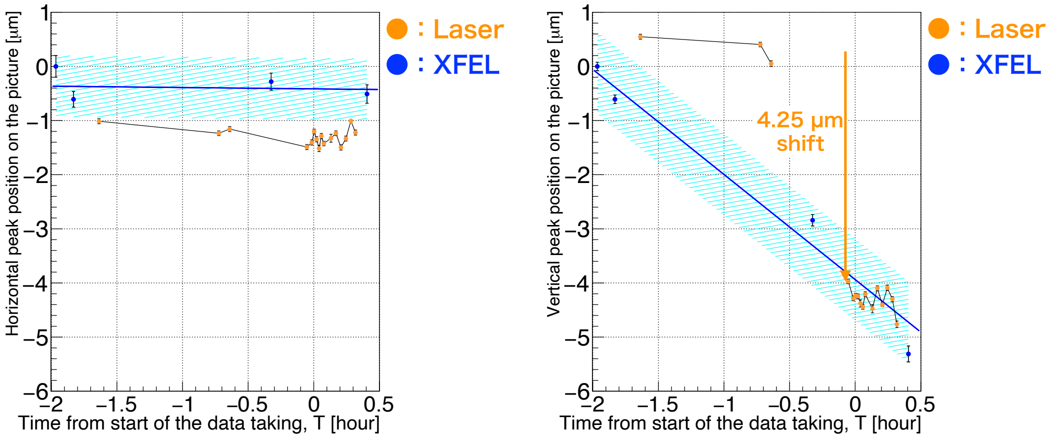

Figure 5.7: Drifts of the peaks of the laser the XFEL images on the picture taken with the Camera2. Left: Horizontal direction; Right: Vertical direction.

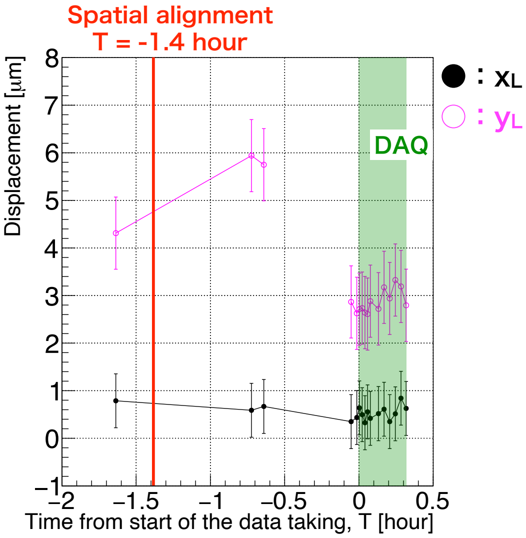

Figure 5.8: Drift of displacement of the laser pulse position against the XFEL pulse position. The green hatch (T = 0 to 0.3 hour) shows the duration of VD search, and the displacements at first 150 pulses of the ten delay time scans and end 150 pulses of the last delay time scan are shown.

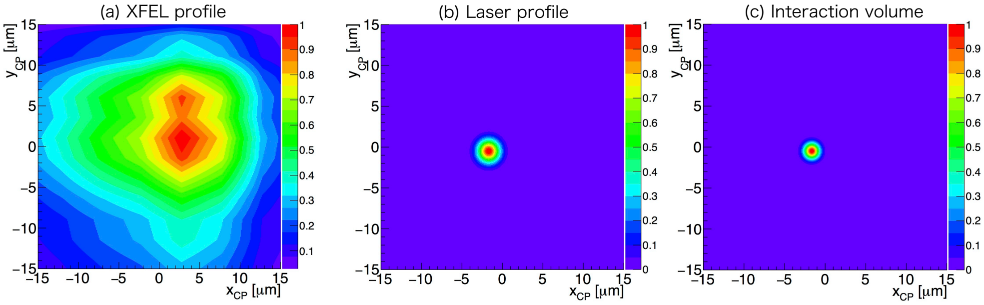
(a) XFEL profile (b) Laser profile (c) Interaction volume

Figure 5.9: Profiles of the laser pulse, the XFEL pulse and the interaction volume at $t_{\mathrm{L}} = 0$. The profiles of both pulses are used for the calculation of the interaction volume. Maximum of three profiles are normalized to 1. (a) XFEL profile, $f_{\mathrm{Xh}}(x_{\mathrm{CP}})f_{\mathrm{Xv}}(y_{\mathrm{CP}})$. (b) Laser profile, $\exp\left[-2\frac{(x_{\mathrm{CP}}-x_{\mathrm{L}})^2}{w_{\mathrm{Lh}}^2} - 2\frac{(y_{\mathrm{CP}}-y_{\mathrm{L}})^2}{w_{\mathrm{L0v}}^2}\right]$.
(c) Interaction volume.

5.2 Expected signal

A distribution of the signal x rays at the collision point is calculated with the following formula,

$$\frac{\mathrm{d}P_{\mathrm{curve}}}{\mathrm{d}x_{\mathrm{CP}}\mathrm{d}y_{\mathrm{CP}}\mathrm{d}\cos\theta} = \frac{\tilde{I}_{\mathrm{IV}}(x_{\mathrm{CP}}, y_{\mathrm{CP}})}{\int \tilde{I}_{\mathrm{IV}}(x_{\mathrm{CP}}, y_{\mathrm{CP}})\mathrm{d}x_{\mathrm{CP}}\mathrm{d}y_{\mathrm{CP}}} \left.\frac{\mathrm{d}P}{\mathrm{d}\cos\theta}\right|_{\Theta_x=\Theta_{nx},\Theta_y=\Theta_{ny}}. \tag{5.1}$$

with

$$\begin{align} \tilde{I}_{\mathrm{IV}}(x_{\mathrm{CP}}, y_{\mathrm{CP}}) =& f_{\mathrm{Xh}}(x_{\mathrm{CP}})f_{\mathrm{Xv}}(y_{\mathrm{CP}}), \tag{5.2} \\ & \times \left(\exp\left[-2\frac{(x_{\mathrm{CP}}-x_{\mathrm{L}})^2}{w_{\mathrm{Lh}}^2} - 2\frac{(y_{\mathrm{CP}}-y_{\mathrm{L}})^2}{w_{\mathrm{Lv}}^2}\right]\right)^2, \tag{5.3} \\ & \tag{5.4} \end{align}$$

where $\tilde{I}_{\mathrm{IV}}(x_{\mathrm{CP}}, y_{\mathrm{CP}})$ is an interaction volume considering the measured XFEL profile. Equation (5.1) is obtained by replacing $I_{\mathrm{IV}}(x_{\mathrm{CP}}, y_{\mathrm{CP}})$ in the fraction in Eq. (2.12) with $\tilde{I}_{\mathrm{IV}}(x_{\mathrm{CP}}, y_{\mathrm{CP}})$.

Figure 5.9 (c) shows the interaction volume at $t_{\mathrm{L}} = 0$. The XFEL profile and the laser profile used for the calculation are also shown in Fig. 5.9 (a) and (b), respectively. The XFEL profile is the product of the horizontal and the vertical profiles, $f_{\mathrm{Xh}}(x_{\mathrm{CP}})f_{\mathrm{Xv}}(y_{\mathrm{CP}})$. The laser profile is a two-dimensional Gaussian function, and its peak has the displacements $(x_{\mathrm{L}}, y_{\mathrm{L}})$. The profile of the interaction volume strongly depends on the laser profile since the beam size of the laser is smaller than that of the XFEL. The region $(|x_{\mathrm{CP}}|, |y_{\mathrm{CP}}| < 15\ \mu\mathrm{m})$, which is shown in Fig. 5.9, is used for the analysis.

Figure 5.10 is the expected signal distribution at $t_{\mathrm{L}} = 0$ as a phase space in the vertical direction. The signal has a Gaussian profile of the angular distribution with

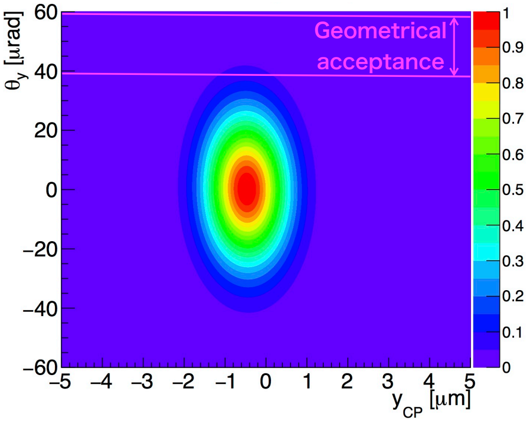

Figure 5.10: The phase space of the signal distribution in the vertical direction. The area between magenta lines shows the geometrical acceptance made by the Slit6.

the divergence of 34 μrad. Due to the curvature of the XFEL pulse, the angle of the signal x-ray is slightly increased as y_{CP} becomes smaller. The area between the magenta line shows the geometrical acceptance of the signals, which corresponds to the opening of the Slit6. The interaction probability is $P = 2.1 \times 10^{-22}/1$ x-ray, and an acceptance A which is the ratio of the signals through the geometrical acceptance is $A = 9.5 \times 10^{-3}$, and the number of expected signal x rays is $n_{\mathrm{QED}} = NPA = 7.0 \times 10^{-15}$ photons/pulse.

The timing distributions of the interaction probability, the acceptance and the expected signal x rays are shown in Fig. 5.11 and Fig. 5.12, respectively. These parameters are calculated in the region where the laser size was observed ($|z| \leq 30$ μm). The interaction probability becomes large around $t_{\mathrm{L}} = 0$ since the interaction probability mainly depends on the effective pulse energy of the laser. Since the divergence of the signal is inversely proportional to the beam size of the laser, the acceptance is large in the region ($t_{\mathrm{L}} < 0$) where the beam size is small. The distribution of the number of expected signal x rays is obtained as the product of distributions of the interaction probability and the acceptance.

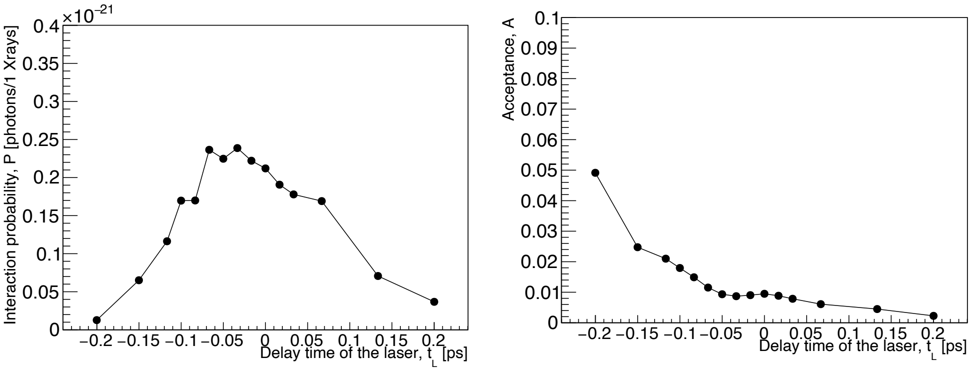

Figure 5.11: Timing distributions of interaction probability P and acceptance A.

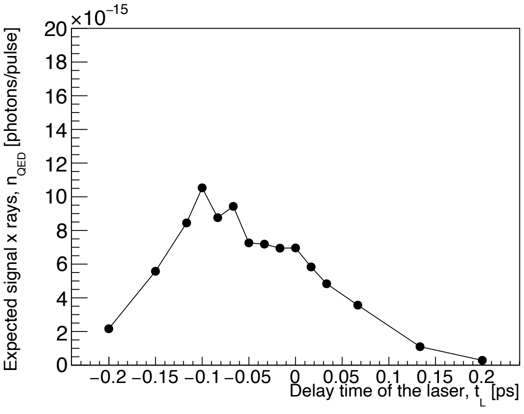

Figure 5.12: Timing distribution of the number of expected signal x rays n_{QED}.

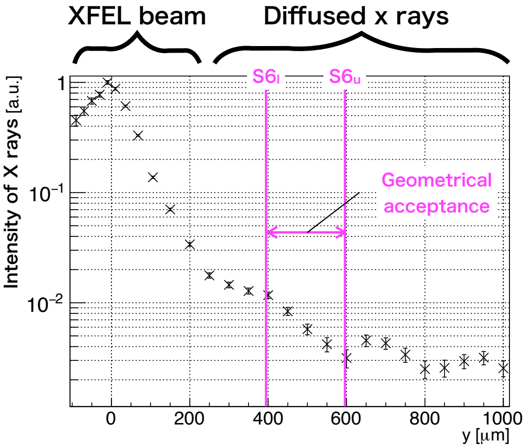

Figure 5.13: The distribution of the intensity of x rays at the Slit6. The area between magenta lines shows the geometrical acceptance by the Slit6.

5.3 BG sources

BGs in the VD experiment are x rays passing the geometrical acceptance by the Slit6 and derive from the x rays of the XFEL pulse. BGs are divided as follows:

i X-ray which has a large angle.

When the XFEL pulse is focused, x rays at the tail of the beam profile get a large angle and become the BG. Since the shaper absorbs this BG, this BG is negligible.

ii Diffused x-ray by the beamline optics.

A part of the x rays in the XFEL pulse is diffused when materials of the transmission-type optics have a non-uniformity and when the TRM and transmission-type optics have the roughness on the surface.

iii Diffracted x-ray by the slit and beamline optics.

X rays is diffracted when the XFEL pulse passes the small aperture of the optics and when the blade of the slit cuts the XFEL pulse or the diffused x rays.

The distribution of the BGs at the Slit6 is shown in Fig 5.13. When the Slit4 is opened, the distribution of x rays is measured by the knife-edge scan of the lower blade of the Slit6. The XFEL beam, which corresponds to the large angle x-ray (i), has a gaussian distribution and is dominant near the beam axis. The diffused x-ray (ii) has a larger divergence than the XFEL beam and is dominant at a region away from the beam axis.

The region where the diffused x-ray is dominant is better for the geometrical acceptance. The geometrical acceptance is shown by the magenta lines. Since the divergence of the signal is larger than the XFEL beam and smaller than the

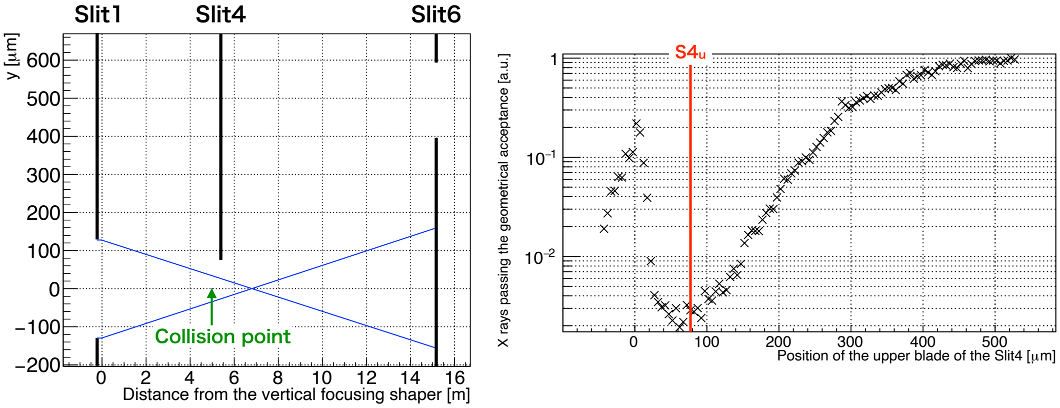

Figure 5.14: (Right) The schematic of the position of the slits. The horizontal axis is the distance from the vertical focusing shaper. The blue line shows the edge of the light ray of the XFEL beam. (Left) The data of the knife-edge scan by the upper blade of the Slit4.

diffused x-ray, the region where the diffused x-ray begins to dominate has a large signal-to-noise ratio.

The position of the upper blade of the Slit4 is optimized to minimize the BGs. Figure 5.14(Left) shows the position of the slits during the data acquisition. Figure 5.14(Right) is the data of the knife-edge scan by the upper blade of the Slit4. The vertical axis shows the number of the BGs passing the geometrical acceptance. The horizontal axis is the position of the edge of the upper blade of the Slit4. When the blade is closed (When the coordinate of the horizontal axis becomes small), the number of diffused x rays is decrease. Whereas the number of diffracted x rays (iii) increase since the diffused x-ray is diffracted by the blade. The diffracted x-ray becomes the dominant BG when the position the blade is near to the beam axis ($\sim 20\ \mu$m). The blade is set at the position with fewer BGs shown as the red line.

5.4 Timing distribution of detected x rays

The number of x rays detected by the PD is shown in Fig. 5.15. The number of x rays of each pulse is shown and have about 40% of the intensity fluctuation (RMS) at each step. The normalized number of detected x rays is shown in Fig. 5.16 as the timing distribution. The black and the magenta point are the collision data and the BG data, respectively. Each bin is normalized by the XFEL intensity as follows: i th bin y_i is $y_i =$ (average of detected x rays) $\times N/N_i$, where N_i is the number of photons in the XFEL pulse shown by i th bin in Fig. 5.5. The errors show uncertainties of the measurement of x rays. Both histograms have a 1 ps and a 0.1 ps scale of intensity fluctuations since the XFEL profile slightly fluctuates in 1 minute and 1 second scale. The intensity fluctuation in 1 ps scale is cancelled out by subtracting the BG data from the collision data.

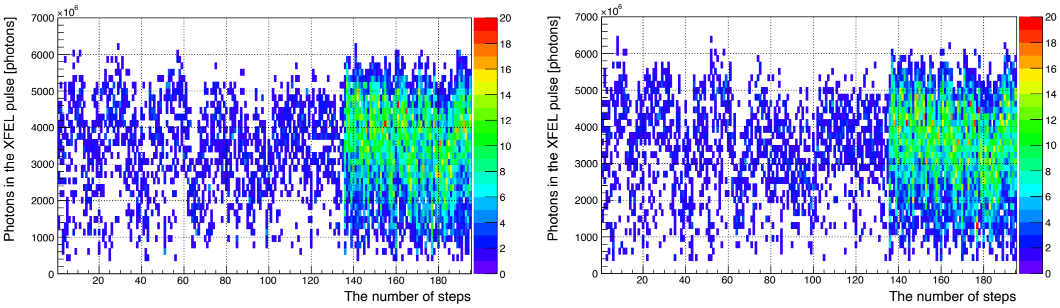

Figure 5.15: Detected x rays of each pulse during the data acquisition. The number of x rays is not normalized by the XFEL intensity. Left: The collision data; Right: The BG data.

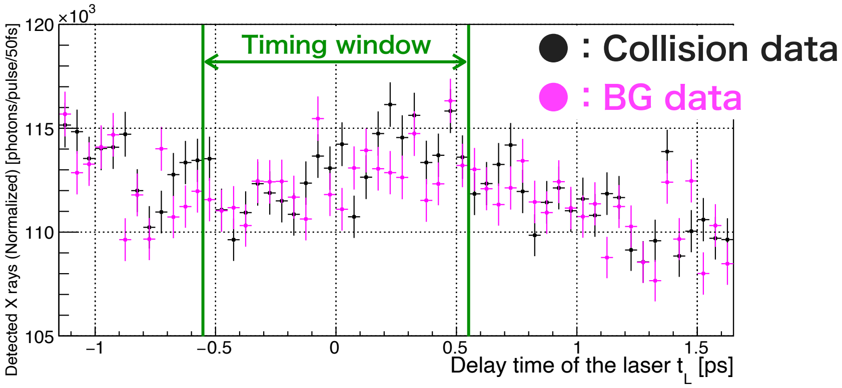

Figure 5.16: The timing distribution of the detected x rays normalized by the XFEL intensity. The black point and the magenta point show the collision data and the BG data, respectively.

Since the intensity fluctuation in a 0.1 ps scale is not canceled out by the subtraction, the standard deviation of this fluctuation, σ_y is estimated by calculating the following value Y

$$Y = \sqrt{\frac{2}{3}}\left(y_i - \frac{y_{i-1}+y_{i+1}}{2}\right). \tag{5.5}$$

Since the width of each bin is enough smaller than 1 ps, Y also has σ_y of the standard deviation, approximately. The calculated σ_y was 1.61×10^3 photons/pulse. The uncertainty of the BG due to the fluctuation of the XFEL profile, σ_{BG}, is also estimated using σ_y. The standard deviation of Y, σ_y, is estimated as $\sigma_y = \sqrt{\sigma^2_{\mathrm{measure}} + \sigma^2_{\mathrm{BG}}}$, where $\sigma_{\mathrm{measure}}$ is the statistical error of each bin due to the measurement of the x rays. $\sigma_{\mathrm{measure}}$ is 0.55×10^3 photons/pulse, and σ_{BG} is 1.51×10^3 photons/pulse.

Figure. 5.17 shows the difference of the BG data from the collision data, n_{xrays}.

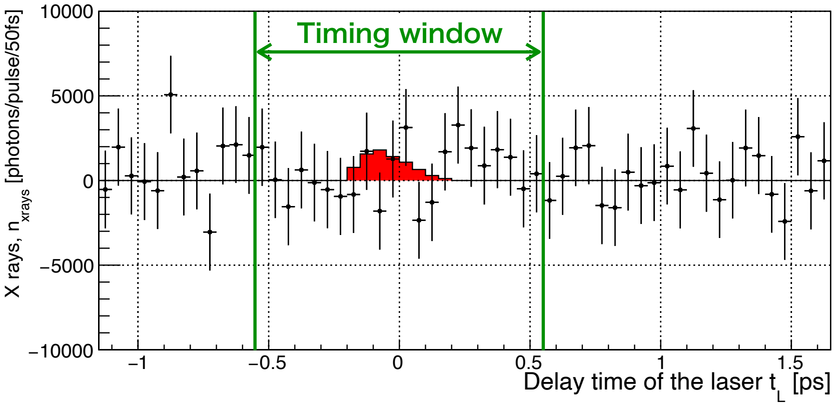

Figure 5.17: The timing distribution of the difference of the number of detected x rays. The difference between the collision data and the BG data is shown. The area between green lines shows the timing window ($|t_{\mathrm{L}}| < 0.55$ fs). The red histogram shows the expected signal of VD, which is multiplied by 2.0×10^{17} for comparison.

The errors show the uncertainties of the BG and the measurement of the x rays. The number of expected signal x rays is shown as a red histogram, which is multiplied by 2.0×10^{17} for the comparison. A sum of the number of x rays in the timing window is $n_{\mathrm{xray,sum}} = (1.02 \pm 1.07(\mathrm{stat}) \pm 0.03(\mathrm{sys})) \times 10^4$ photons. A sum of the number of expected x rays in the timing window is $n_{\mathrm{QED,sum}} = 3.9 \times 10^{-14}$ photons. No evidence for an excess of the number of x rays due to VD was not observed.

5.5 Analysis of the upper limit on VD

An upper limit for the interaction probability is calculated although significant signals are not observed. The limit on the interaction probability is calculated by the ratio of sum of the number of x rays in the timing window, $n_{\mathrm{xray,sum}}$, to the sum of the number of expected x rays in the timing window, $n_{\mathrm{QED,sum}}$, as follows

$$\frac{n_{\mathrm{xray,sum}}}{n_{\mathrm{QED,sum}}}, \tag{5.6}$$

where

$$n_{\mathrm{xray,sum}} = \frac{1}{1.1\ \mathrm{ps}} \int_{-0.55\ \mathrm{ps}}^{+0.55\ \mathrm{ps}} n_{\mathrm{xrays}}\ dt_{\mathrm{L}} \tag{5.7}$$

$$n_{\mathrm{QED,sum}} = \frac{1}{1.1\ \mathrm{ps}} \int_{-0.55\ \mathrm{ps}}^{+0.55\ \mathrm{ps}} n_{\mathrm{QED}}\ dt_{\mathrm{L}}. \tag{5.8}$$

5.5.1 Systematic uncertainties

The parameters n_{xrays} and $n_{\mathrm{QED}}(= NPA)$ have an uncertainty. Table. 5.2 is a summary of systematic uncertainties on $n_{\mathrm{QED,sum}}$ due to observed parameters.

Table 5.2: The summary of systematic uncertainties on $n_{\mathrm{QED,sum}}$ calculated from the experimental parameters.

Parameters	Uncertainties on $n_{\mathrm{QED,sum}}$
The number of x rays in the XFEL pulse, N	-0.7% / 0.7%
Pulse energy of the laser, W	-22% / 25%
Horizontal beam size of the laser, w_{Lh}	-13% / 17%
Vertical beam size of the laser, w_{Lv}	-55% / 109%
Horizontal beam size of the XFEL, w_{Xh}	-14% / 19%
Vertical beam size of the XFEL, w_{Xv}	-21% / 33%
Pulse durations, $\tau_{\mathrm{L}}, \tau_{\mathrm{X}}$	-25% / 42%
Horizontal displacement, x_{L}	-9%
Vertical displacement, y_{L}	-43% / 36%
Lower blade position of Slit6, $S6_{\mathrm{l}}$	-4% / 5%
Upper blade position of Slit6, $S6_{\mathrm{u}}$	-0.3% / 0.3%
Distance from the collision point to the Slit6, $D_{\mathrm{CP/Slit6}}$	-2% / 2%
Distance from the shaper to the collision point, z_{X}	-1% / 0.9%
Minimum XFEL beam size, w_{X0v}	-0.5% / 0.9%
Divergence of the XFEL beam, φ	-0.1% / 0.2%

Each uncertainty is subsequently explained in the following subsections.

Uncertainty on the x rays: n_{xrays}

The x rays n_{xrays}, which is the difference between the collision data and the BG data, has uncertainties due to the fluctuation of BGs and the measurement of x rays. Dominant error source is the statistical uncertainty due to the fluctuation of the BG. The uncertainty on $n_{\mathrm{xrays,sum}}$ is $\pm 1.07 \times 10^4$ photons in total.

uncertainty on the number of x rays in the XFEL pulse: N

The number of the x rays in the XFEL pulse, N, has uncertainty due to the calibration of the SCM and the intensity fluctuation. The uncertainties on N and $n_{\mathrm{QED,sum}}$ are both $\pm 0.7\%$.

uncertainty on the pulse energy of the laser: W

The pulse energy of the laser, W, has $\pm 12\%$ uncertainty. The dominant uncertainty is caused due to the estimation of the ratio of the effective pulse energy. Since P is proportional to W^2, $n_{\mathrm{QED,sum}}$ is nearly proportional to W^2. The uncertainty on $n_{\mathrm{QED,sum}}$ is ${}^{+25\%}_{-22\%}$.

Uncertainty on the horizontal beam size of the laser pulse: w_{Lh}

The horizontal beam size of the laser pulse, w_{Lh}, has $\pm 0.2\ \mu$m uncertainty due to systematic uncertainties of the measurement dedicated in Sec 3.2.3. From Eq. (2.6), P is nearly proportional to $1/w_{\mathrm{Lh}}\sqrt{w_{\mathrm{Lh}}^2 + 2w_{\mathrm{Xh}}^2} \sim 1/(w_{\mathrm{Lh}} w_{\mathrm{Xh}}),\ (w_{\mathrm{Lh}} \ll w_{\mathrm{Xh}})$. $n_{\mathrm{QED,sum}}$ is roughly proportional to $1/w_{\mathrm{Lh}}$, and the uncertainty on $n_{\mathrm{QED,sum}}$ is $^{+17\%}_{-13\%}$.

Uncertainty on the vertical beam size of the laser pulse: w_{Lv}

The vertical beam size of the laser pulse, w_{Lv}, also has $\pm 0.2\ \mu$m uncertainty. P is nearly proportional to $1/w_{\mathrm{Lh}}\sqrt{w_{\mathrm{Lv}}^2 + 2w_{\mathrm{Xv}}^2} \sim 1/w_{\mathrm{Lv}},\ (w_{\mathrm{Lv}} \ll w_{\mathrm{Xv}})$ and has about $\pm 10\%$ uncertainty.

The acceptance A is also affected. The geometrical acceptance corresponds to between 2.3σ and 3.5σ in the Gaussian angular distribution of the signals. Since the divergence (2σ) is proportional to $\frac{\sqrt{w_{\mathrm{Lv}}^2 + 2w_{\mathrm{Xv}}^2}}{w_{\mathrm{Lv}} w_{\mathrm{Xv}}} \sim 1/w_{\mathrm{Lv}}(w_{\mathrm{Lv}} \ll w_{\mathrm{Xv}})$, the divergence has about $\pm 10\%$ uncertainty and A has about $\pm 70\%$ uncertainty. In total, the uncertainty on $n_{\mathrm{QED,sum}}$ is $^{109\%}_{-55\%}$.

Uncertainty on the horizontal beam size of the XFEL pulse: w_{Xh}

The horizontal beam size of the XFEL pulse is $w_{\mathrm{Xh}} = (22.0 \pm 3.5)\ \mu$m. The systematic uncertainties come due to conditions for the measurement and the analysis of the knife edge scan data. P is nearly proportional to $1/w_{\mathrm{Lh}}\sqrt{w_{\mathrm{Lh}}^2 + 2w_{\mathrm{Xh}}^2} \sim 1/(w_{\mathrm{Lh}} w_{\mathrm{Xh}}),\ (w_{\mathrm{Lh}} \ll w_{\mathrm{Xh}})$. The uncertainty on $n_{\mathrm{QED,sum}}$ is $^{+19\%}_{-14\%}$.

Uncertainty on the vertical beam size of the XFEL pulse: w_{Xv}

The vertical beam size of the XFEL pulse is $w_{\mathrm{Xv}} = (14.8 \pm 4.3)\ \mu$m. As with w_{Xh}, w_{Xv} has the systematic uncertainties and the dependence on P. Although w_{Xv} also depends on A, the uncertainty of A is less than 2%. In total, the uncertainty on $n_{\mathrm{QED,sum}}$ is $^{+33\%}_{-21\%}$.

Uncertainty on the signal estimation due to both pulse durations: τ_{L}, τ_{X}

The signal has uncertainty depending on both pulse durations since the signal is calculated under the limit that both pulse durations are short ($\tau_{\mathrm{L}},\ \tau_{\mathrm{X}} \to 0$). The beam size of the laser slightly depends on z. Since the beam size of the laser is not constant during the interaction due to both pulse durations, P and the divergence of the signal have uncertainties. The maximum and the minimum sizes of the laser beam during the interaction are calculated by assuming both pulses to be the square wave in the time-domain. The laser beam size, P and A change about $\pm 10\%$, $\pm 10\%$ and $\pm 30\%$, respectively. In total, the uncertainty on $n_{\mathrm{QED,sum}}$ is $^{+42\%}_{-25\%}$.

Uncertainty on the horizontal displacement: x_{L}

The horizontal displacement is $x_{\mathrm{L}} = (0.5 \pm 4.2)$ μm. The uncertainties come from the spatial alignment and the drift of the laser position. P is proportional to $\exp\left[-4\frac{x_{\mathrm{L}}^2}{w_{\mathrm{Lh}}^2+2w_{\mathrm{Xh}}^2}\right]$, which shows how well both pulses overlap. The uncertainty on $n_{\mathrm{QED,sum}}$ is -9%.

Uncertainty on the vertical displacement: y_{L}

The vertical displacement is $y_{\mathrm{L}} = (2.9 \pm 3.8)$ μm. As with x_{L}, y_{L} has the systematic uncertainties and the dependence on P. The uncertainty on P is about -30%.

A is also affected due to the wavefront curvature of the XFEL pulse. Depending on y_{L}, the effect of the wavefront curvature shifts the median of the angle distribution of the signals. The shift of the angle is ± 2.1 μrad, and A is changed by about $\pm 20\%$. In total, the uncertainty on $n_{\mathrm{QED,sum}}$ is ${}^{+36\%}_{-43\%}$.

Uncertainty on the position of the blade of the Slit6: $S6_{\mathrm{l}}$, $S6_{\mathrm{u}}$

The positions of the Slit6 blade are $S6_{\mathrm{l}} = (395.0 \pm 3.0)$ μm and $S6_{\mathrm{u}} = (596.2 \pm 4.4)$ μm. The uncertainties come from the accuracy of the measurement of the beam axis position and give the uncertainty of the size of the opening. The uncertainties on $n_{\mathrm{QED,sum}}$ due to $S6_{\mathrm{l}}$ and $S6_{\mathrm{u}}$ are ${}^{+5\%}_{-4\%}$ and ${}^{+0.3\%}_{-0.3\%}$, respectively.

Uncertainty on the distance from the collision point to the Slit6: $D_{\mathrm{CP/Slit6}}$

The distance from the collision point to the Slit6, $D_{\mathrm{CP/Slit6}}$, is 10.18 m. The half-size of slits in the z-direction, 36 mm, is taken as the uncertainty of the position of the blades. This uncertainty changes the selection angle for the signals. The uncertainty on $n_{\mathrm{QED,sum}}$ is ${}^{+0.9\%}_{-1\%}$.

Uncertainty from the XFEL beam parameters: z_{X}, w_{X0v}, φ

The distance between the XFEL focal spot and the collision point $z_{\mathrm{X}} = (1.76 \pm 0.08)$ m, the minimum XFEL beam size $w_{\mathrm{X0v}} = (3.1 \pm 1.8)$ μm, and the divergence of the XFEL beam $\varphi = (10.6 \pm 1.1)$ μrad, are determined by fitting the beam sizes in the z-direction. The wavefront curvature of the XFEL pulse depends on these parameters. The uncertainties on $n_{\mathrm{QED,sum}}$ from these three parameters are ${}^{+1\%}_{-0.9\%}$, ${}^{+0.9\%}_{-0.5\%}$, and ${}^{+0.2\%}_{-0.1\%}$, respectively.

5.5.2 Final result

The uncertainties shown above are taken into account, and $n_{\mathrm{QED,sum}} = (3.9^{+6.1}_{-2.5}) \times 10^{-14}$ photons and $n_{\mathrm{xray,sum}} = (1.02 \pm 1.07) \times 10^4$ photons are obtained.

In order to calculate the limit, $n_{\mathrm{QED,sum}}$ and $n_{\mathrm{xrays,sum}}$ are estimated with Monte Carlo calculations. As the probability density functions of the experimental parameters to estimate $n_{\mathrm{QED,sum}}$, a gaussian functions which have the standard deviation same with the error of the experimental parameters is used. As the probability density function of $n_{\mathrm{xrays,sum}}$, the following function is used

$$f(n_{\mathrm{xrays,sum}}) = \begin{cases} 0 & n_{\mathrm{xrays,sum}} < 0 \\ e^{-\frac{(n_{\mathrm{xrays,sum}} - n_0)^2}{2\sigma_{\mathrm{un}}^2}} & 0 \leq n_{\mathrm{xrays,sum}} \end{cases} \tag{5.9}$$

where $n_0 = 1.02 \times 10^4$ photons and $\sigma_{\mathrm{un}} = 1.07 \times 10^4$ photons are the measured value of $n_{\mathrm{xrays,sum}}$ and its uncertainty, respectively. The obtained upper limit with the 90% confidence level is

$$\frac{n_{\mathrm{xrays,sum}}}{n_{\mathrm{QED,sum}}} < 2.3 \times 10^{18} \quad (90\%\ \mathrm{C.L.}). \tag{5.10}$$

Chapter 6

Discussion and prospect

6.1 Significance of the experimental result

The focus of my research was to establish a new VP search method to improve signal statistics which limit the experimental sensitivity in the previous experiments [6–9, 21]. I established the new VP search method via VD search, which has not been searched so far and can generate large signal statistics. In the VD search, creating the focused laser field which generates large signals and colliding the laser field with the sensitive XFEL pulse are needed. I made the optical system using the adaptive optics and focused the laser pulse to $\sim \mu$m level. Using the Au foil and the GaAs crystal, I developed the precise alignment techniques, and both pulses were collided. The shaper was also developed, and BG was suppressed.

The first limit on VP by the VD experiment was obtained using the established method. This is also the first experimental restriction on VD, and the new information about the properties of VP regarding VD was obtained in addition to photon-photon scattering and vacuum birefringence.

In Fig. 6.1, experimental sensitivities against VP by the VD experiment and previous experiments are compared. The signals expected by QED, which is proportional to the square of the fine structure constant α^2, is normalized to 1, and a sensitivity to the signals are shown with 90% C.L. The sensitivity of the VD experiment is better than the photon-photon scattering experiment using x rays [6]. Due to the insufficient suppression of BGs, the sensitivity is not good compared with the vacuum birefringence experiments. The sensitivity of the previous experiments is limited by various reasons, for example, BGs which can not be reduced and few signal statistics. The VD experiment is very promising because the improvement of the sensitivity and the observation of VP are expected by upgrades.

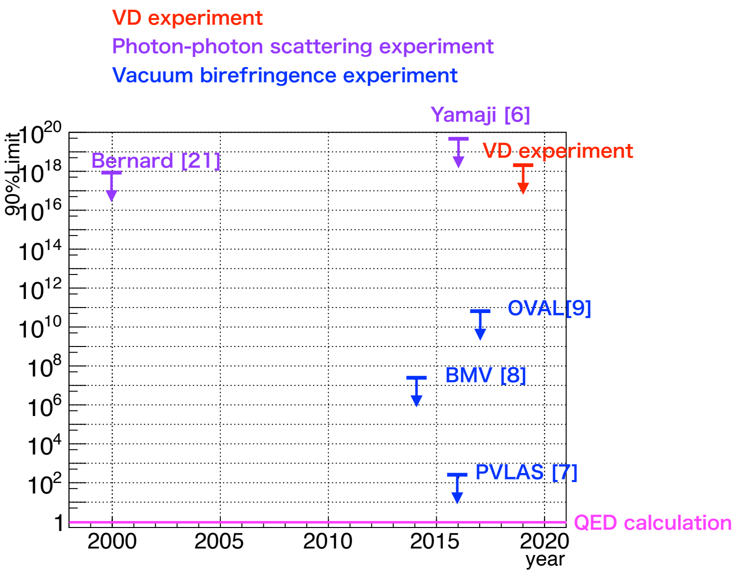

Figure 6.1: Comparison of experimental sensitivities against VP.

6.2 Future prospects

6.2.1 Upgrades for the future experiment

Since the developments of the experimental techniques were taken as the top-priority issue in my research, there is still room for improvement of the experimental parameters for the future experiment. Plans for upgrades of the experimental parameters are summarized in the following. The experimental parameters in my research and after the upgrades are summarized in Tab. 6.1. By considering the upgrades, the experimental sensitivity of the VD experiment improves 9.5×10^{20} times.

Table 6.1: Expected gain factor by upgrades. The extinction ratio is the accuracy of the polarizer to separate an s-polarized x-ray and a p-polarized x-ray.

Parameters		My research	Upgrade	Gain
Laser pulse energy [J]		0.47×10^{-3}	12.5	7.0×10^{8}
Polarizer (Extinction ratio)		-	2×10^{-10}	5.0×10^{9}
Beam sizes [μm]	Laser	1.9 and 1.9	1.0 and 1.0	2.7×10^{2}
	XFEL	22.0 and 14.8	2.0 and 2.0	
Total				9.5×10^{20}

Laser pulse energy

The 500-TW laser is installed in SACLA. The laser has 12.5 J of the pulse energy. Using this laser, the sensitivity is improves $(12.5\ \mathrm{J}/0.47\ \mathrm{mJ})^2 = 7 \times 10^8$ since the interaction probability P is proportional to the pulse energy. The beam size of the laser becomes larger (120 mm diameter) to avoid the thermal damage to the optics.

Beam sizes

The beam sizes of the XFEL and the laser are needed to decrease to 2 μm and 1 μm to increase the interaction probability, respectively. The XFEL beam size is decreased by colliding the XFEL pulse at its focus. The laser beam size is decreased by using a DM which is already installed in the 500-TW laser system. In my research, the laser beam size was larger than 1 μm because the astigmatism of the laser pulse was too large to correct higher-order aberration by the DM. If the 500-TW laser pulse has a large lower-order aberration, the large aberration is needed to be cancelled out by other optics. Otherwise, a DM which has more actuators is needed. A group which uses the DM with three times more actuators achieves 1 μm of the focus size [40].

The interaction probability P is proportional to $P \sim \frac{1}{w_{\mathrm{Lh}} w_{\mathrm{Lv}}} \frac{1}{\sqrt{w_{\mathrm{Lh}}^2 + 2w_{\mathrm{Xh}}^2}} \frac{1}{\sqrt{w_{\mathrm{Lv}}^2 + 2w_{\mathrm{Xv}}^2}}$. By decreasing the beam sizes, the interaction probability increase 2.7×10^2 times.

Background suppression

BGs, which are x rays of the XFEL pulse, are suppressed by its polarization. Since the polarization of a part of diffracted signal x rays is changed, these x rays are separated from BGs by a polarizer and observed. There is a high precision polarizer using the Bragg refection for an x-ray [41]. This polarizer only reflects an s-polarized x-ray with 2×10^{-10} of the accuracy. With the polarizer, the experimental sensitivity improves 5×10^9. The development of this polarizer was already started, and a prototype polarizer is shown in App. B.

Alignments

The accuracy of the spacial alignment is needed smaller than the XFEL beam size (2 μm). The accuracy is mainly determined by the uncertainty of both pulse positions. The uncertainty of the XFEL position shown in Tab.4.1 is 1/7 of the beam size. This uncertainty becomes smaller than the beam size since this uncertainty decreases proportionally to the beam size. The uncertainty of the laser position is caused due to the instability of the shape of the irradiation trace. The cause of the instability is thought to be the roughness on the surface of the Au foil (a few μm) or the softness. Research and development of the spacial alignment using a flat and a hard foil are necessary.

The improvement of the time alignment accuracy is also important since the jitter between the 500-TW laser and the XFEL (56 fs) is smaller than that for the

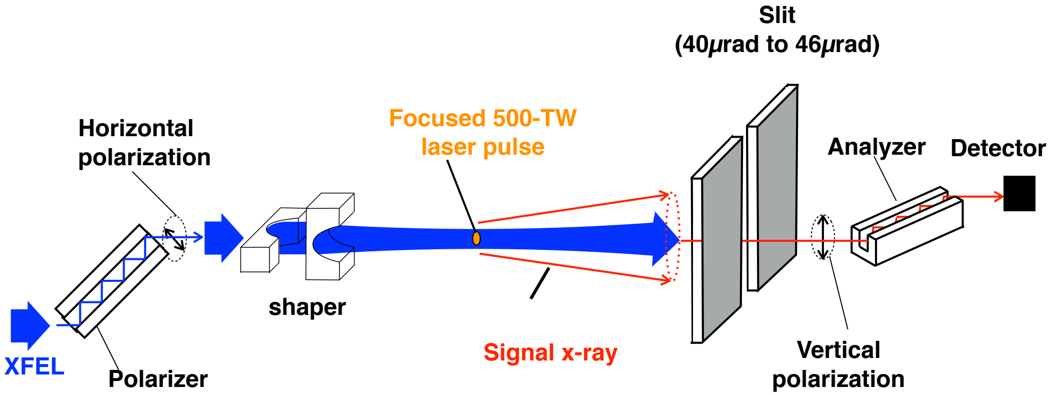

Figure 6.2: Experimental setup of the future experiment.

0.6-TW laser (~ 300 fs). The accuracy of the time alignment is mainly determined by the uncertainty of the position of the GaAs crystal. Since this uncertainty can be suppressed by a simple measurement and iterations, for example, a measurement of levelness of the chamber, the accuracy of the time alignment decrease to about 40 fs, which is the total of uncertainties due to other sources.

6.2.2 Future experiment

The future experiment is designed by considering the upgrades. The experimental setup is shown in Fig. 6.2. The purity of the polarization of the XFEL pulse is enhanced by the polarizer, and the XFEL pulse is focused to 2 μm by the shapers. The 500-TW laser pulse is focused to 1 μm and collided with the XFEL pulse. X rays are diffracted with 66 μrad of the divergence, and 9/130 of the diffracted x rays are changed its polarization. These x rays are separated from BGs by the slit and the analyzer which is the same device with the polarizer. The separated x rays are observed by a photon detector. Considered experimental parameters are summarized in Tab 6.2.

The selection angle for the signals by the slit is 40 μrad to 46 μrad since the incident angle at which the analyzer reflects photons is $45^\circ \pm 3$ μrad. The suppression of BGs by silt is 1×10^{-5} by considering the decrease of the width of the selection angle (20 μrad $\rightarrow$ 6 μrad). The suppression by analyzer is 2×10^{-10}, and the total suppression of BGs is 2×10^{-15}. In order to estimate the expected signals, a perfect alignment ($x_\mathrm{L} = y_\mathrm{L} = t_\mathrm{L} = 0$) is assumed, and a loss due to a jitter between the XFEL beam and the 500-TW laser (56 fs, RMS) is considered. The repetitions of the XFEL and the laser are 60 Hz and 1 Hz, which are maximum repetitions of the XFEL of SACLA and the 500-TW laser, respectively. The collision data and the BG data are measured with 1 Hz and 59 Hz, respectively. The expected signals reach 4.1^{+3}_{-2}(stat) photons with 20 days of the data acquisition. In contrast, the expected BGs are 1.6 ± 0.2(stat) photons, and VD is observed.

6.2.3 Requirement for the future experiment

In the future experiment, a decrease of the energy bandwidth of the XFEL is required (30 eV → 1 eV, FWHM) since the energy width of x rays reflected by the polarizer is very small (50 meV). The energy bandwidth can be decreased to 1 eV, which is the target value of the future experiment, by a technique called as a seeding of the XFEL [42], and SACLA achieved to decrease the energy bandwidth to 3 eV by the seeding. More improvement in the operation of the XFEL with the seeding technique is required.

Birefringence of the shaper should be lower than that of the polarizer in order not to generate BGs. The shaper may have birefringence though the shaper is made of Si crystal, which has symmetric structure. There are two possibilities of birefringence sources. One is the roughness of the surface on the shaper ($\sim 1\ \mu$m), which is made due to the etching process. The other is a solution for the etching, which is left on the surface of the shaper. These possibilities should be studied.

Table 6.2: The summary of the experimental parameters of the future experiment.

		Parameters
Laser parameters	Laser	500-TW laser
	Pulse energy	12.5 J
	Beam size	1 μm
	Polarization	45° from horizontal direction
	Repetition	1 Hz
XFEL parameters	Photon energy	8.4 keV
	Pulse energy	4×10^{11} photons/pulse
	Beam size	2 μm
	Polarization	horizontal
	Repetition	60 Hz
	Divergence	20 μrad
	Energy bandwidth	1 eV (FWHM)
	Transmittance of shaper	6.3% (for two shapers)
	Transmittance of polarizer	1.8%
BG separation	Slit : Direction of aperture	horizontal
	Selection angle	40 μrad to 46 μrad
	Fraction of BGs through slit	1×10^{-5}
	Polarizer : Crystal plane	Si(511)
	A number of reflections	Eight times
	Extinction ratio	2×10^{-10}
Signal parameters	Divergence	66 μrad
	Acceptance by slit	1.1%
	Diffraction efficiency of analyzer	0.40 (for eight times reflections)
	Interaction probability	7.2×10^{-12}
	Ratio of polarization flipped x rays	9/130
	Loss due to Jitter	0.34
	Rate of collision data	1 Hz
	Rate of BG data	59 Hz
	Time of data acquisition	20 days
	Expected signals	4.1 photons
	Expected BGs	1.6 ± 0.2(stat) photons

Chapter 7

Conclusion

This thesis reported a vacuum polarization search with the new experimental scheme. Diffraction of the XFEL pulse under the strong laser pulse was searched. This new scheme has not been done due to the difficultly of the collision of both pulses. To resolve this problem and establish the experimental method of the VD experiment, I developed

1. the precise spatial and temporal alignment techniques with 4 μm and 160 fs accuracies
2. the precise control system of the laser phase by the deformable mirror to focus the laser pulse
3. the novel x-ray optics, shaper, to suppress BGs.

In addition, I derived the theoretical formula of the signal distribution of the VD. The effective signal distribution was calculated by considering the effects which have not been considered so far, for example, the divergence of the XFEL beam.

The first experimental search for VD was performed at the beamline 3 of SACLA, XFEL facility. The 0.6-TW laser is focused to 1.9 μm, and the 22.0 $\mu\text{m}\times14.8\ \mu$m of the XFEL pulse is precisely collided with the laser pulse by the developed alignment techniques. No significant signals are observed, and the 90% C.L. upper limit on the interaction probability of VD is obtained. The limit is obtained by the ratio of the number of the observed x rays, $n_{\text{xray,sum}}$, to the number of the expected x rays in QED, $n_{\text{QED,sum}}$, as follows:

$$\frac{n_{\text{xrays,sum}}}{n_{\text{QED,sum}}} < 2.3 \times 10^{18} \quad (90\%\ \text{C.L.}). \tag{7.1}$$

This is the first limit on VP by the VD experiment and is also the first experimental restriction on VD.

This experiment also demonstrates the feasibility of the observation of VD. VD can be observed in the future experiment with the XFEL and the 500-TW laser of SACLA. Requirements for the alignment accuracy and the BG suppression in the future experiment will be achieved by the developed techniques and optics.

Appendix A

Shaper

In this section, the effect of the suppression of the BG in the VD experiment by the shaper is discussed. BGs in a VD search is a part of probe x rays passing through the opening of the slit which is set in front of an x-ray detector. These x rays are divided into three cases, as follows:

i X rays which have a large angle

ii Diffused x rays by the beamline optics

iii Diffracted x rays by the slit and beamline optics

It is possible to block the direct path to the opening for these x rays by using the slit. However, enough suppression of BG x rays is impossible because the slit which blocks the direct path causes new diffracted x rays (iii). For example, Fresnel diffraction is typical diffraction caused by the slit. The shaper is developed to remove BG x rays without the new diffraction of x rays.

Since the shaper smoothly shapes the beam profile different from the slit, diffraction is not caused. Figure A.1 shows the XFEL beam profile shaped by the shaper. The blue point is the shaped beam profile, and the grey point is a raw XFEL beam. The data was measured at SPring-8 beamline 19. Only one dimension of the profile is shaped. Since the shaped profile has a good gaussian profile, the diffraction due to the shaping is well suppressed. The red line is a gaussian function fitted to the shaped profile and drown with 7σ of the width. Since the shaper also works as the focusing lens, the diffraction due to the aperture of the focusing lens (iii) is also decreased.

Since the shaper selectively absorbs the photon at the tail of the beam profile, a divergence of the beam is decreased, and the large angle x rays (i) is suppressed. Figure A.2 shows the focused XFEL beam of the SACLA BL3. The light blue points show the focused beam by the shaper, and the orange points show the focused beam by the beryllium (Be) lens equipped at the EH2. The blue and the red lines are fitting functions of the Gaussian beam, respectively. By using the

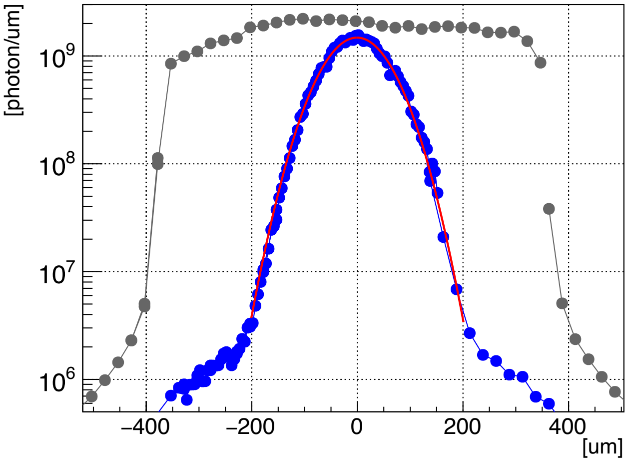

Figure A.1: Comparison of the raw XFEL profile (grey) and the profile shaped by the shaper (blue). The red line is the fitted gaussian function drown with 7σ of the width.

shaper, the divergence of the beam is strongly decreased (65 μrad→ 10 μrad). Due to this effect, BG x rays are decreased about 3 digits.

The shaper also decreases the diffused x rays (ii). The Be lens, which is a typical x-ray lens, has vacancies and distortion in the lens since it is created by pressing the material. The x-ray is diffused by the vacancy and the distortion. Whereas the shaper does not have the vacancy and the distortion since it is made of a Si crystal. Figure A.3 shows the x-ray camera images of the focused XFEL beam by the Be lens and the shaper. The focused XFEL beam by the Be lens has many diffused x rays around the peak. By focusing the XFEL with the shaper, the diffused x rays are well suppressed. The diffused x rays are caused due to pillars which are created during the etching process.

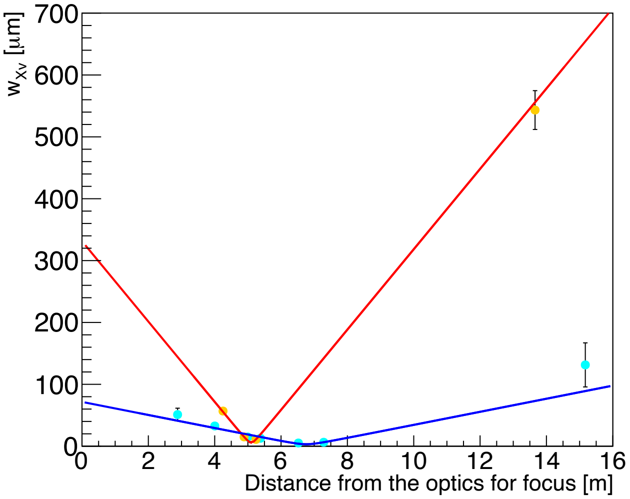

Figure A.2: Comparison of the XFEL beams focused by the shaper (light blue point) and the Be lens (orange point). The blue and the red lines are fitting functions of the Gaussian beam, respectively.

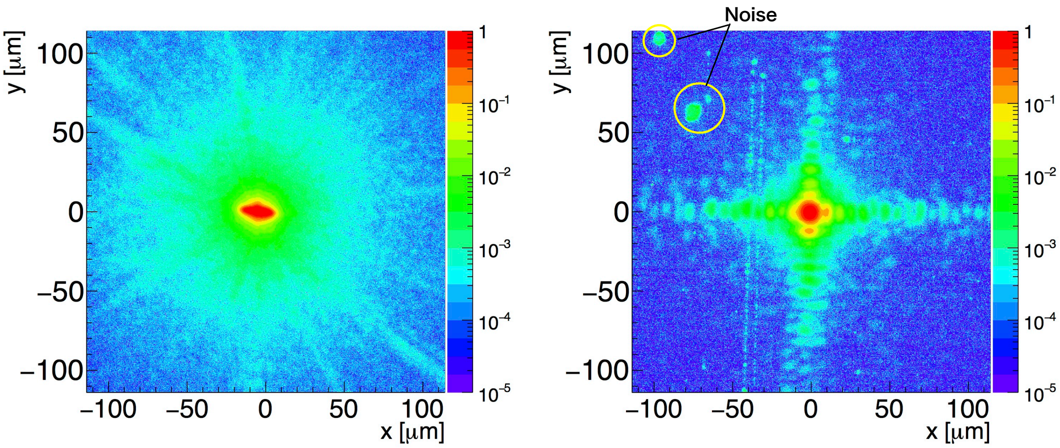

Figure A.3: The x-ray camera images of the focused XFEL beam by the Be lens and the shaper. The color of the image means the intensity of the x rays. (Left) The image focused by the Be lens. (Right) The image focused by the shaper. The spots circled by yellow lines are noise due to the thermal damage of the fluorescent screen of the x-ray camera.

Appendix B

Polarizer

The polarizer has been developed for the future VD experiment. The target value of the extinction ratio is $< 2 \times 10^{-10}$. Amount of light transmitted through the polarizer is depend on the direction of the polarization of lights. The extinction ratio is the ratio of minimum and maximum amount of light transmitted through the polarizer. The polarizer in the x-ray region is a reflective type optics made of a crystal. X rays enter the polarizer with Brewster's angle (45°), which is the incident angle at which only s-polarized x rays are reflected, and reflected by Bragg diffraction. The main cause which makes the extinction ratio worse is the phenomenon called as Multiple beam reflection (MBR). An x-ray is reflected several times in the crystal and emitted to the same direction as the reflection at Brewster's angle.

The polarizer with less MBR is created with the optimization of the crystal plane, the x-ray energy and the azimuth angle of the crystal. Figure B.1 shows the image of the polarizer made of Si crystal. The mirror index of the crystal plane is (511). The polarizer works as a polarizer for an 8.3878 keV x-ray. X rays are reflected eight times to improve the extinction ratio.

The extinction ratio was measured at SPring-8 BL19, which is an x-ray beamline. The azimuth angle and the angle between the polarizer and the analyzer were adjusted. 1.3×10^{-7} of the extinction ratio was obtained with the best alignment of the polarizer and the analyzer. Figure. B.2 shows the change of the extinction ratio when the incident angle of x rays to the analyzer is changed. The polarizer and the analyzer are crossed at $\theta = 0$ μrad.

The obtained extinction ratio is three digits larger than the target value. From the measurement of the dependence against the azimuth angle, it is confirmed that the crystal plane is the same as the designed plane, which has a small effect of MBR. A reason other than MBR makes the extinction ratio worse. One candidate to make the extinction ratio worse is the scattered x-ray by the polarizer. More precise polishing of the polarizer ($\sim$10 nm class roughness on the surface) is considered.

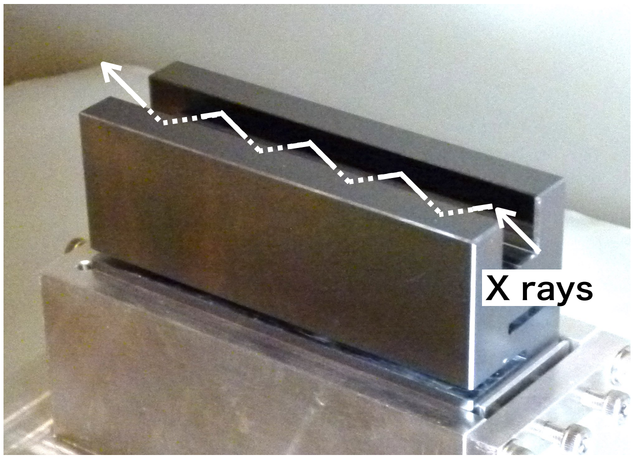

Figure B.1: Polarizer made of Si.

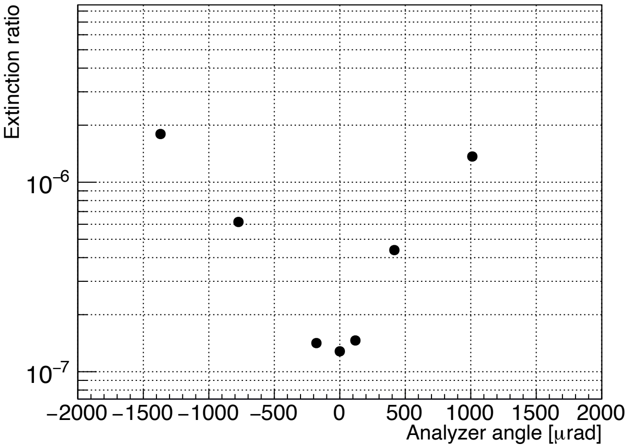

Figure B.2: Extinction ratio as a function of the analyzer position. The analyzer position $\theta = 0$ μrad corresponds to the situation that the analyzer and the polarizer are in the crossed position.

Appendix C

List of symbols

Table C.1: List of main symbols used in this theses.

Symbol	Attribution
A	Acceptance of the signal x rays
c	The speed of light in vacuum
$D_{\mathrm{CP/Slit6}}$	Distance from the collision point to the Slit6
e	Electron mass
f_{Xh}	Horizontal XFEL profile at the collision point
f_{Xv}	Vertical XFEL profile at the collision point
$\hbar$	Reduced Planck constant
I_{IV}	Interaction volume
$\tilde{I}_{\mathrm{IV}}$	Interaction volume considering the measured XFEL profile
n_{QED}	The number of expected signal x rays
$n_{\mathrm{QED,sum}}$	The sum of n_{QED} in the timing window
n_{xrays}	The difference of the number of x rays between the collision data and the BG data
$n_{\mathrm{xrays,sum}}$	The sum of n_{xrays} in the timing window
N	The number of x rays in the XFEL pulse
P	Interaction probability
$S6_{\mathrm{l}}$	Lower blade position of Slit6
$S6_{\mathrm{u}}$	Upper blade position of Slit6
t_{L}	Delay time of the laser pulse
W	Pulse energy of the laser
x_{CP}	x coordinate at the collision point
x_{L}	Horizontal displacement of the laser pulse against the XFEL pulse
y_{CP}	y coordinate at the collision point
y_{L}	Vertical displacement of the laser pulse against the XFEL pulse
z_{X}	Distance from the shaper to the collision point
α	Fine structural constant
θ	Diffraction angle against z-axis

continued on the next page...

continued from the previous page...

Symbol	Attribution
θ_x	Diffraction angle in the horizontal direction
θ_y	Diffraction angle in the vertical direction
μ_0	The magnetic permeability of vacuum
$\tau_{\rm L}$	Pulse duration of the laser pulse
$\tau_{\rm X}$	Pulse duration of the XFEL pulse
φ	Divergence of the XFEL beam
$w_{\rm Lh}$	Horizontal beam size of the laser
$w_{\rm Lv}$	Vertical beam size of the laser
$w_{\rm X0v}$	Minimum XFEL beam size
$w_{\rm Xh}$	Horizontal beam size of the XFEL
$w_{\rm Xv}$	Vertical beam size of the XFEL

End.

Table C.2: List of abbreviations used in this theses.

Abbreviation	Long form
BG	Background
DM	Deformable mirror
EH	Experimental hatch
FWHM	Full width at half maximum
LH	Laser hatch
ND	Neutral density filter
OAP	Off axis parabolic mirror
PD	Photo diode
RMS	Root mean square
ROI	Region of interesting
SACLA	SPring-8 angstrom compact free electron laser
SCM	Screen monitor
TM	Timing monitor
TRM	Total reflection mirror
VD	Vacuum diffraction
VP	Vacuum polarization
WFS	Wavefront sensor
XFEL	X-ray free electron laser

End.

Acknowledgements

I would like to express the deepest appreciation to my supervisor Prof. Shoji Asai and my former supervisor Prof. Hiroshi Sakamoto for providing me with the opportunity of this work. I was supported by their encouragements and assistance.

I also wish to express my great appreciation to Prof. Toshio Namba for his many guidance. He gave me a lot of comments and useful advice every time. My aim is to create logic, slide and paper which do not need to be corrected by him.

I am thankful to Prof. Takayuki Yamazaki, Dr. Toshiaki Inada and Dr. Tomohiro Yamaji. Daily discussions and experiments with them and sincere supports make me grow up as a researcher.

The experiment has been performed in cooperation with researchers of SPring-8/SACLA. I would like to express my gratitude to Prof. Kenji Tamasaku, Prof. Yoshiki Komura, Prof. Yuichi Inubushi, Prof. Tadashi Togashi and Prof. Toshinori Yabuuchi for providing technical advice and supports to my experimental studies at SACLA. I would like to thank Prof. Shigeki Owada, Dr. Ichiro Inoue, Dr. Taito Osaka, Prof. Makina Yabashi and Prof. Tetsuya Ishikawa for useful discussions about x-ray physics and optics. I gratefully thank all engineers for kind supports to my experimental studies.

I would also like to thank Prof. Kentaro Kawai for collaborative research for the development of the new x-ray optics. Thanks to him and his techniques, the shaper was created.

I also express my sincere gratitude to Prof. Felix Karbstein for theoretical discussion. My research started with his paper.

I would like to thank Prof. Katsumi Midorikawa, Prof. Akira Ishida, Prof. Yoshio Kamiya, Prof. Kenji Shu and Shusei Kamioka for useful discussion. I would also like to thank all staffs and colleagues of the University of Tokyo for their kind supports.

Finally, my family are my emotional supports. I really appreciate what they have done for me. Thank you.

Bibliography

[1] ATLAS Collaboration, Observation of a new particle in the search for the Standard Model Higgs boson with the ATLAS detector at the LHC, Physics Letters B **716**(1), 1–29 (2012).

[2] CMS Collaboration, Observation of a new boson at a mass of 125 GeV with the CMS experiment at the LHC, Physics Letters B **716**(1), 30–61 (2012).

[3] V. P. Nair, *Quantum Field Theory*, Springer, 2005.

[4] B. King and T. Heinzl, Measuring Vacuum Polarisation with High Power Lasers, High Power Laser Science and Engineering **4**, 92 (2016).

[5] F. Moulin, D. Bernard, and F. Amiranoff, Photon-photon elastic scattering in the visible domain, Zeitschrift für Physik C **72**, 607–611 (1996).

[6] T. Yamaji, T. Inada, T. Yamazaki, T. Namba, S. Asai, T. Kobayashi, K. Tamasaku, Y. Tanaka, Y. Inubushi, K. Sawada, M. Yabashi, and T. Ishikawa, An experiment of X-ray photon–photon elastic scattering with a Laue-case beam collider, Physics Letters B **763**, 454–457 (2016).

[7] G. Zavattini, F. D. Valle, A. Ejlli, W.-T. Ni, U. Gastaldi, E. Milotti, R. Pengo, and G. Ruoso, Intrinsic mirror noise in Fabry-Perot based polarimeters: the case for the measurement of vacuum magnetic birefringence, The European Physical Journal C **78**, 585 (2018).

[8] M. T. Hartman, R. Battesti, and C. Rizzo, Characterization of the Vacuum Birefringence Polarimeter at BMV: Dynamical Cavity Mirror Birefringence, IEEE Transactions on Instrumentation and Measurement **68**(6), 2268–2273 (June 2019).

[9] X. Fan, S. Kamioka, T. Inada, T. Yamazaki, T. Namba, S. Asai, J. Omachi, K. Yoshioka, M. Kuwata-Gonokami, A. Matsuo, K. Kawaguchi, K. Kindo, and H. Nojiri, The OVAL experiment: a new experiment to measure vacuum magnetic birefringence using high repetition pulsed magnets, The European Physical Journal D **71**, 308 (2017).

[10] R. D. Peccei and H. R. Quinn, CP Conservation in the Presence of Pseudoparticles, Physical Review Letters **38**(25), 1440–1443 (1977).

[11] L. Maiani, R. Petronzio, and E. Zavattini, Effects of nearly massless, spin-zero particles on light propagation in a magnetic field, Physics Letters B **175**(3), 359–363 (1986).

[12] M. I. Dobroliubov and A. Y. Ignatiev, Millicharged particles, Phys. Rev. Lett. **65**, 679–682 (Aug 1990).

[13] J. Schwinger, On Gauge Invariance and Vacuum Polarization, Phys. Rev. **82**, 664–679 (Jun 1951).

[14] W. G. Unruh, Notes on black-hole evaporation, Phys. Rev. D **14**, 870–892 (Aug 1976).

[15] W. Heisenberg and H. Euler, Consequences of the Dirac Theory of Positrons, Zeit. f. Phys **98**, 714–732 (1936).

[16] R. Baier and P. Breitenlohner, The Vacuum Refraction Index in the Presence of External Fields, Il Nuovo Cimento B (1965-1970) **47**(1), 117–120 (January 1967).

[17] O. Halpern, Scattering Processes Produced by Electrons in Negative Energy States, Phys. Rev. **44**, 855–856 (Nov 1933).

[18] B. De Tollis, Dispersive Approach to Photon-Photon Scattering, Il Nuovo Cimento (1955-1965) **32**(3), 757–768 (May 1964).

[19] B. De Tollis, The scattering of photons by photons, Il Nuovo Cimento (1955-1965) **35**(4), 1182–1193 (Feb 1965).

[20] A. L. Hughes and G. E. M. Jauncey, An Attempt to Detect Collisions of Photons, Phys. Rev. **36**, 773–777 (Aug 1930).

[21] D. Bernard, F. Moulin, F. Amiranoff, A. Braun, J. Chambaret, G. Darpentigny, G. Grillon, S. Ranc, and F. Perrone, Search for stimulated photon-photon scattering in vacuum, The European Physical Journal D **10**, 141–145 (2000).

[22] T. Inada, T. Yamaji, S. Adachi, T. Namba, S. Asai, T. Kobayashi, K. Tamasaku, Y. Tanaka, Y. Inubushi, K. Sawada, M. Yabashi, and T. Ishikawa, Search for photon–photon elastic scattering in the X-ray region, Physics Letters B **732**, 356–359 (2014).

[23] F. D. Valle, A. Ejlli, U. Gastaldi, G. Messineo, E. Milotti, R. Pengo, G. Ruoso, and G. Zavattini, The PVLAS experiment: measuring vacuum magnetic birefringence and dichroism with a birefringent Fabry-Perot cavity, The European Physical Journal C **76**, 24 (2016).

[24] A. Cadène, P. Berceau, M. Fouché, R. Battesti, and C. Rizzo, Vacuum magnetic linear birefringence using pulsed fields: status of the BMV experiment, The European Physical Journal D **68**, 16 (2014).

[25] A. D. Piazza, K. Z. Hatsagortsyan, and C. H. Keitel, Light Diffraction by a Strong Standing Electromagnetic Wave, Physical Review Letters **97**, 083603 (2006).

[26] M. Yabashi, H. Tanaka, K. Tono, and T. Ishikawa, Status of the SACLA Facility, Applied Sciences **7**(6), 604 (2017).

[27] T. Heinzl, B. Liesfeld, K.-U. Amthor, H. Schwoerer, R. Sauerbrey, and A. Wipf, On the observation of vacuum birefringence, Optics Communications **267**(2), 318–321 (2006).

[28] F. Karbstein, H. Gies, M. Reuter, and M. Zepf, Vacuum birefringence in strong inhomogeneous electromagnetic fields, Physical Review D **92**, 071301(R) (2015).

[29] F. Karbstein and C. Sundqvist, Probing vacuum birefringence using x-ray free electron and optical high-intensity lasers, Physical Review D **94**, 013004 (2016).

[30] F. Karbstein, Vacuum birefringence in the head-on collision of x-ray free-electron laser and optical high-intensity laser pulses, Physical Review D **98**, 056010 (2018).

[31] B. King, A. D. Piazza, and C. H. Keitel, A matterless double slit, Nature Photonics **4**, 92–94 (2010).

[32] D. Tommasini and H. Michinel, Light by light diffraction in vacuum, Physical Review A **82**, 011803(R) (2010).

[33] G. Y. Kryuchkyan and K. Z. Hatsagortsyan, Bragg Scattering of Light in Vacuum Structured by Strong Periodic Fields, Physical Review Letters **107**, 053604 (2011).

[34] Y. Seino, T. Inada, T. Yamazaki, T. Namba, and S. Asai, New estimation of the curvature effect for the X-ray vacuum diffraction induced by an intense laser field, Progress of Theoretical and Experimental Physics **2020**(7) (07 2020), 073C02.

[35] H. Ohashi, M. Yabashi, K. Tono, Y. Inubushi, T. Sato, T. Togashi, Y. Senba, T. Koyama, H. Yumoto, K. Miyokawa, T. Ohsawa, S. Goto, and T. Ishikawa, Beamline mirrors and monochromator for X-ray free electron laser of SACLA, Nuclear Instruments and Methods in Physics Research A **710**, 139–142 (2013).

[36] T. Katayama, S. Owada, T. Togashi, K. Ogawa, P. Karvinen, I. Vartiainen, A. Eronen, C. David, T. Sato, K. Nakajima, Y. Joti, H. Yumoto, H. Ohashi, and M. Yabashi, A beam branching method for timing and spectral characterization of hard X-ray free-electron lasers, Structural Dynamics **3**(3), 034301 (2016).

[37] H. Harmand, R. Coffee, M. R. Bionta, M. Chollet, D. French, D. Zhu, D. M. Fritz, H. T. Lemke, N. Medvedev, B. Ziaja, S. Toleiks, and M. Cammarata, Achieving few-femtosecond time-sorting at hard X-ray free-electron lasers, Nature Photonics **7**, 215–218 (2013).

[38] http://xfel.riken.jp/eng/users/bml04-11.html .

[39] Web page of HAMAMATSU for PD (S3590-09).

[40] V. Yanovsky, V. Chvykov, G. Kalinchenko, P. Rousseau, T. Planchon, T. Matsuoka, A. Maksimchuk, J. Nees, G. Cheriaux, G. Mourou, and K. Krushelnick, Ultra-high intensity-300-TW laser at 0.1 Hz repetition rate, Optics Express **16**(3), 2109–2114 (2008).

[41] B. Marx, K. S. Schulze, I. Uschmann, T. Kämpfer, R. Lötzsch, O. Wehrhan, W. Wagner, C. Detlefs, T. Roth, J. Härtwig, E. Förster, T. Stöhlker, and P. G, G, High-Precision X-Ray Polarimetry, Physical Review Letters **110**, 254801 (2013).

[42] I. Inoue, T. Osaka, T. Hara, T. Tanaka, T. Inagaki, T. Fukui, S. Goto, Y. Inubushi, H. Kimura, R. Kinjo, H. Ohashi, K. Togawa, K. Tono, M. Yamaga, H. Tanaka, T. Ishikawa, and M. Yabashi, Generation of narrow-band X-ray free-electron laser via reflection self-seeding, Nature Photonics **13**(5), 319–322 (2019).